© 2020. Published by The Company of Biologists Ltd | Development (2020) 147, dev193946. doi:10.1242/dev.193946

STEM CELLS AND REGENERATION

RESEARCH ARTICLE

Reactive oligodendrocyte progenitor cells (re-)myelinate the regenerating zebrafish spinal cord

Vasiliki Tsata[1,*], Volker Kroehne[1,‡], Daniel Wehner[1,2,3,‡], Fabian Rost[1,4], Christian Lange[1], Cornelia Hoppe[1], Thomas Kurth[5], Susanne Reinhardt[6], Andreas Petzold[6], Andreas Dahl[6], Markus Loeffler[7], Michell M. Reimer[1,§] and Michael Brand[1,§]

ABSTRACT

Spinal cord injury (SCI) results in loss of neurons, oligodendrocytes and myelin sheaths, all of which are not efficiently restored. The scarcity of oligodendrocytes in the lesion site impairs re-myelination of spared fibres, which leaves axons denuded, impedes signal transduction and contributes to permanent functional deficits. In contrast to mammals, zebrafish can functionally regenerate the spinal cord. Yet, little is known about oligodendroglial lineage biology and re-myelination capacity after SCI in a regeneration-permissive context. Here, we report that, in adult zebrafish, SCI results in axonal, oligodendrocyte and myelin sheath loss. We find that OPCs, the oligodendrocyte progenitor cells, survive the injury, enter a reactive state, proliferate and differentiate into oligodendrocytes. Concomitantly, the oligodendrocyte population is re-established to pre-injury levels within 2 weeks. Transcriptional profiling revealed that reactive OPCs upregulate the expression of several myelination-related genes. Interestingly, global reduction of axonal tracts and partial re-myelination, relative to pre-injury levels, persist at later stages of regeneration, yet are sufficient for functional recovery. Taken together, these findings imply that, in the zebrafish spinal cord, OPCs replace lost oligodendrocytes and, thus, re-establish myelination during regeneration.

KEY WORDS: Zebrafish, Oligodendrocyte progenitor cells, CNS injury, (Re-)myelination, CNS regeneration, Spinal cord

INTRODUCTION

Local death of mature myelinating oligodendrocytes is one of the first events that occurs after spinal cord injury (SCI) in mammals (Totoiu and Keirstead, 2005), impeding both the survival and function of denuded axons (Ludwin and Maitland, 1984). This is followed by a secondary damage, which involves excitotoxicity and a deleterious immune response, resulting in a subacute phase of cell death and prolonged loss of oligodendrocytes that develops in a time-dependent manner and persists chronically (Crowe et al., 1997; Guest et al., 2005; Papastefanaki and Matsas, 2015).

Limited re-myelination after insult may occur by recruitment of oligodendrocyte progenitor cells (OPCs), as oligodendrocytes are post-mitotic and do not contribute to re-myelination (Franklin et al., 1997; Keirstead and Blakemore, 1997). Although OPCs are highly dynamic and respond to injury by rapidly migrating and proliferating (Hughes et al., 2013), oligodendrocytes are not sufficiently replaced and the formation of new myelin from newly generated oligodendrocytes is either incomplete or, in the case of chronically demyelinating lesions, insufficient (Keirstead et al., 1998). This has been attributed to progenitor depletion over the course of damage-progression, age-related impairment of OPC recruitment and differentiation, and axonal dystrophy (Raine and Cross, 1989; Sim et al., 2002; Mason et al., 2004; Neumann et al., 2019). Another possibility is that the inhibitory environment of the injury scar perturbs migration and differentiation of OPCs into oligodendrocytes (Fok-Seang, 1995; Plemel, 2013). Interestingly, transplantation of myelinating progenitors (Cao et al., 2005; Keirstead et al., 2005) as well as activation of endogenous progenitor pools (Llorens-Bobadilla et al., 2020) have been shown to enhance myelination capacity and, hence, improve conduction recovery after injury. Given the importance of myelination in the mechanical, trophic and metabolic support of spared and regrown axons (Fünfschilling et al., 2012), this highlights the importance of a holistic understanding of OPC biology towards enhancing re- and *de novo* myelination, and potentially functional recovery, after injury of the central nervous system (CNS).

In contrast to mammals, adult zebrafish possess a high CNS regenerative capacity and efficiently regenerate injured brain and spinal cord tissue (Becker et al., 1997; Kaslin et al., 2008; Reimer et al., 2008; Kroehne et al., 2011). For the latter, remarkable recovery of function has been documented. Although spinal cord transection results in full paralysis caudal to the lesion site (Becker et al., 2004; Mokalled et al., 2016), zebrafish are able to regain swimming activity by 42 days post lesion (dpl), a process that is dependent on regeneration of axonal tracts across the lesion site (Becker et al., 2004).

Although, the transcription factors as well as the molecular mechanisms governing lineage progression of oligodendroglial cells and myelination are largely conserved between zebrafish and mammals, differences might exist in the dynamics of OPC/oligodendrocyte responses after injury, which may contribute to the different regenerative outcomes. However, to date, a detailed analysis of oligodendroglial cell behaviour after SCI in a vertebrate of high regenerative capacity is lacking.

Here, we have used an adult zebrafish spinal cord transection model (Becker et al., 1997) to provide novel insight into OPC responses in a

[1]Center for Regenerative Therapies Dresden TU Dresden (CRTD) and Cluster of Excellence, Physics of Life (PoL), TU Dresden, Dresden 01307, Germany. [2]Max Planck Institute for the Science of Light, Erlangen 91058, Germany. [3]Max-Planck-Zentrum für Physik und Medizin, Erlangen 91058, Germany. [4]Center for Information Services and High Performance Computing, TU Dresden, Dresden 01062, Germany. [5]Center for Molecular and Cellular Bioengineering (CMCB), TU Dresden, Technology Platform, Dresden 01307, Germany. [6]Dresden Genome Center c/o Center for Regenerative Therapies TU Dresden (CRTD), TU Dresden, Dresden 01307, Germany. [7]Center for Advancing Electronics Dresden (cfaed)/Dresden Center for Nanoanalysis (DCN), TU Dresden, Dresden 01062, Germany.
*Present address: Developmental Biology, Clinical, Experimental Surgery and Translational Research Center, Biomedical Research Foundation Academy of Athens, Athens 11527, Greece.
‡These authors contributed equally to this work

§Authors for correspondence (michael.brand@tu-dresden.de; Michell.Reimer@web.de)

V.T., 0000-0002-7741-9702; V.K., 0000-0002-5610-0866; D.W., 0000-0003-2880-4759; A.D., 0000-0002-2668-8371; M.B., 0000-0001-5711-6512

Handling Editor: Steve Wilson
Received 14 June 2020; Accepted 28 October 2020

Development (2020) 147, dev193946. doi:10.1242/dev.193946

regenerative context. We find that, after spinal cord transection, myelinating oligodendrocytes are lost close to the injury site. OPCs appear to largely survive the primary and secondary damage, enter an activated state, increase proliferation and differentiate into oligodendrocytes, allowing mature oligodendrocytes to re-establish their population within 2 weeks post-injury. Transcriptome analysis of OPCs after lesion reveals that activated OPCs upregulate genes related to OPC differentiation and maturation into myelinating oligodendrocytes. Hence, adult zebrafish OPCs represent a highly dynamic cell population that contributes to the regeneration response of the injured spinal cord.

RESULTS

Oligodendrocyte number transiently decreases after SCI

To characterize the dynamics of oligodendroglial lineage cell response after injury in the adult zebrafish spinal cord, we first analysed oligodendrocytes using the transgenic Tg(*mbp*:eGFP) line. In this line, eGFP expression is driven by the myelin basic protein (*mbp*) promoter, labelling oligodendrocyte cell bodies and myelin sheaths of actively myelinating mature oligodendrocytes (Jung et al., 2010). After spinal cord transection, the number of *mbp*:eGFP$^+$ oligodendrocytes was significantly reduced at 3 and 7 dpl in the spared spinal cord tissue immediately adjacent to the transection site, when compared with sham controls (Fig. 1A,B). Furthermore, myelin sheaths were damaged by the acute insult (Fig. 1A, insets). Thus, *mbp*:eGFP$^+$ oligodendrocytes are lost early after SCI. At 14 dpl and 42 dpl, the number of *mbp*:eGFP$^+$ oligodendrocyte cell bodies returned to pre-injury levels (Fig. 1A,B), coinciding with active axonal regrowth (Kuscha et al., 2012) and recovery of locomotor function, respectively (Becker et al., 2004). The loss of *mbp*:eGFP$^+$ oligodendrocytes both at 3 dpl (not shown) and at 7 dpl occurred in a spatially confined manner, within a 700 µm zone around the transection site [±350 µm along the rostrocaudal (RC) axis] (Fig. 1C; Fig. S1), henceforth referred to as the lesion site (Fig. 1G). Thus, in the zebrafish spinal cord, *mbp*:eGFP$^+$ cell loss and damage is confined to a highly restricted zone in the immediate vicinity of the transection site – consistent with previous reports describing the spatial confinement of reactive neurogenesis proximal to the site of injury in adult zebrafish (Reimer et al., 2008).

To investigate whether the loss of *mbp*:eGFP$^+$ expression reflects loss of oligodendrocytes due to cell death, we used the TUNEL assay to quantify dying cells. To exclude the possibility that dying cells are missed due to the distance from the lesion site or their rapid clearance, we examined cell death within 100 µm from the transection site and lesion epicentre (Fig. S2) as early as 4 h post lesion (hpl) (Fig. 1D). Indeed, we could readily detect TUNEL$^+$ cells at 4 hpl and at 1 and 2 dpl (Fig. 1E), confirming sufficient sensitivity of the assay. Interestingly, the number of *mbp*:eGFP$^+$/TUNEL$^+$ cells remained very low at all investigated time-points, as compared to sham controls (Fig. 1F). This raises the possibility that *mbp*:eGFP$^+$ cells survive the injury. However, we cannot exclude the possibility that the absence of *mbp*:eGFP$^+$/TUNEL$^+$ cells is due to an altered transcriptional activity of GFP-reporter expression. Taken together, in the adult zebrafish spinal cord, the *mbp*:eGFP$^+$ oligodendrocyte population recovers after injury, in a process that begins early after the acute insult and continues until the restoration of *mbp*:eGFP$^+$ cell numbers.

SCI results in reduction of axonal tracts, myelin sheath loss and altered tissue architecture

Because the number of *mbp*:eGFP$^+$ oligodendrocytes was re-established by 42 dpl in the lesion site, we sought to investigate myelination status at high cellular resolution using transmission electron microscopy (TEM). As the experimental set-up used in this study (full transection) precludes the unambiguous differentiation between re-myelination of previously demyelinated axons, *de novo* myelination of regrown axons and spared or non-transected axons, we henceforth refer to this process as (re-)myelination.

To examine the effect of SCI at the ultrastructural level, we first quantified the number of axons in the rostral part of the lesion site at 7 and 42 dpl and in sham controls. To avoid bias of small- and/or large-diameter axons, we performed the analysis in two zones of the adult zebrafish spinal cord, at defined dorsal and ventral positions (see schematic in Fig. 2). At 7 dpl, massive tissue disruption was evident in both zones examined, as indicated by the perturbed tissue architecture, the global loss of compact myelin sheaths and the presence of cellular and myelin debris, likely as a result of the primary impact of the transection (Fig. 2A,B, 7 dpl). Furthermore, we found that in both ventral and dorsal areas of the spinal cord, the total number of axons (both non-myelinated and myelinated) was reduced by half, when compared with sham controls. Although tissue integrity was restored at 42 dpl, the number of axons remained lower when compared with sham controls (Fig. 2C). To further monitor myelination dynamics, we also quantified the percentage of myelinated axons after injury (Fig. 2D). In both zones examined, we found that the percentage of myelinated axons was significantly reduced at 7 dpl. Interestingly, although detectable recovery was observed from 7 to 42 dpl, the percentage of myelinated axons remained lower when compared with sham controls at 42 dpl. Moreover, axonal and myelin sheath loss was accompanied by a marked response of the macrophage/microglia that were detected close to the transection site, and were closely associated with myelin and lipid debris, often engulfing them (arrowheads in Fig. 2E).

Taken together, these data show that almost 50% of axonal tracts rostral to the transection site are lost after injury, which persists until at least 42 dpl. Furthermore, although myelin pattern partially recovers, the percentage of myelinated axons does not fully return to pre-injury levels. Given the distinct poor regenerating capacity of ascending fibres and that descending tracts substantially retract after transection and before re-extension (Becker and Becker, 2001; Becker et al., 2005), the axons detectable in the areas examined (see Fig. 2A-D) likely represent regrowth of new axonal segments. This provides tentative evidence for re-myelination of regenerated axonal segments after SCI.

To determine the anatomical quality of myelin formation after injury, we determined the G ratio of axons (diameter of axon/diameter of axon plus myelin), as a readout for myelin thickness (Fig. 2F). Interestingly, G-ratio analysis revealed variability of (re-)myelination patterns among analysed fish (Fig. 2G,H). Specifically, in two out of three fish, the diameter of myelinated axons was higher at 42 dpl when compared with sham controls, while spinal cord transection resulted in lower frequency of medium-sized myelinated axons (Fig. 2I), when compared with sham controls (Fig. 2J). These data suggest that, at 42 dpl, (re-)myelination is not yet complete, or is partial, and that regeneration extent varies between individual fish.

Interestingly, besides the distinct (re-)myelination pattern observed, SCI resulted in a markedly altered tissue architecture in the regenerated spinal cord that persisted at 42 dpl. Severed Mauthner axons did not recover, and some myelin/lipid debris remained close to the lesion site, in spite of the restoration of tissue integrity (Fig. 3A, yellow arrowheads). Moreover, at 42 dpl, a large proportion of the spinal cord parenchyma was covered by vessels (Fig. 3A, 42 dpl), while the area of the ventricular central canal was

Development (2020) 147, dev193946. doi:10.1242/dev.193946

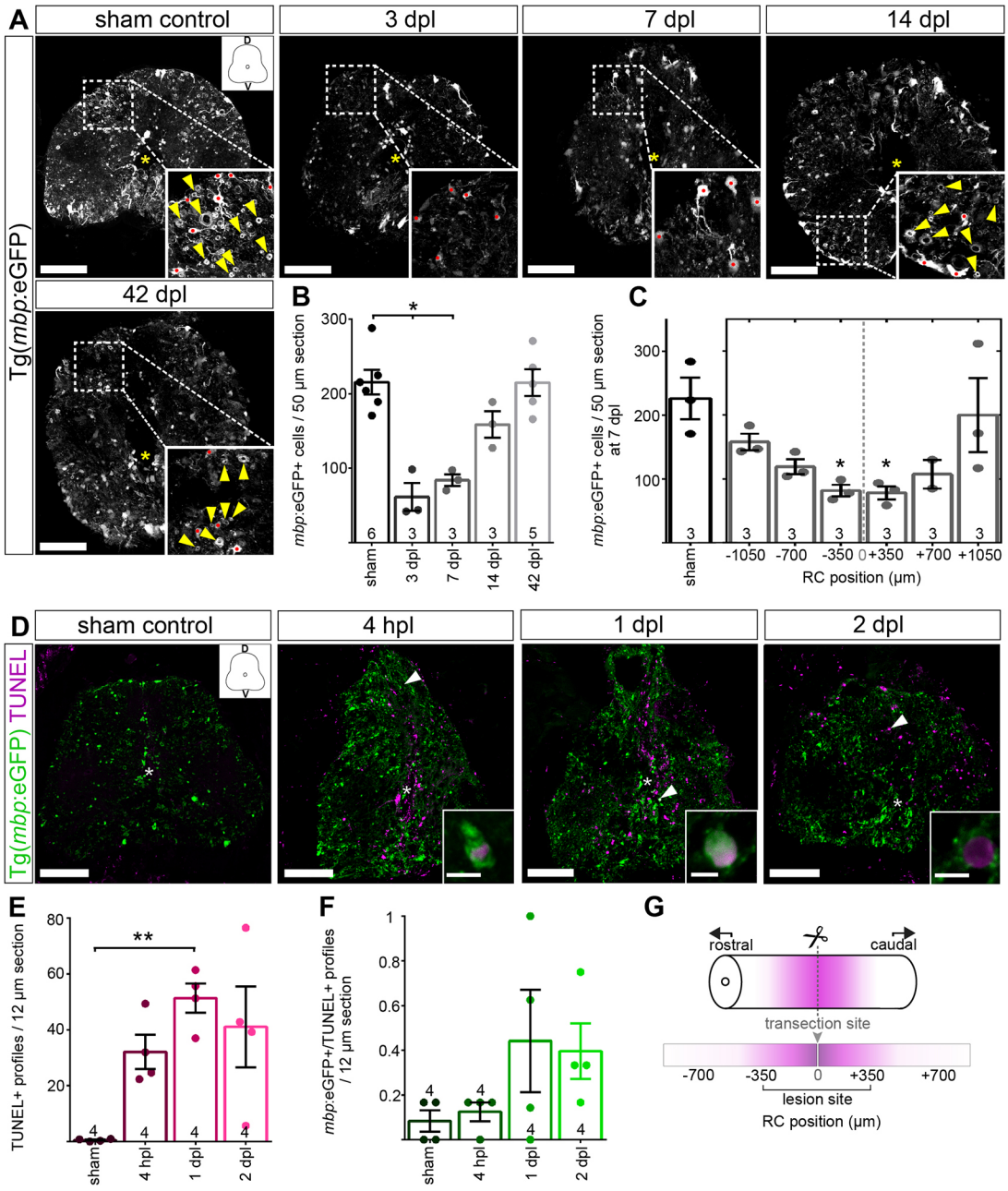

Fig. 1. Oligodendrocyte numbers are transiently decreased and re-established after SCI. (A) *mbp*:eGFP$^+$ oligodendrocyte somata (insets, red dots) and myelin sheaths (insets, yellow arrowheads) are reduced after SCI, but the population is re-established at 14 dpl. Images are maximum intensity projections of transverse sections. D, dorsal; V, ventral. In the overview images, a yellow asterisk indicates the central canal. Scale bars: 100 µm. (B) Stereological quantification of *mbp*:eGFP$^+$ somata 350 µm rostral and caudal to the transection site shows a significant reduction in the number of oligodendrocytes at 7 dpl, compared to sham controls. Evidence of re-myelination is detected as early as 14 dpl (inset, yellow arrowheads). Data are mean±s.e.m. Numbers in the plots indicate the number of experimental animals. *P≤0.05 (Kruskal–Wallis followed by Dunn's multiple comparisons post-hoc test). Significance is shown compared to sham control. (C) Stereological quantification of *mbp*:eGFP$^+$ cells at 7 dpl along the rostrocaudal (RC) axis and around the transection site shows a spatially restricted loss of myelinating oligodendrocytes. Data are mean±s.e.m. Numbers in the plots indicate the number of experimental animals. *P≤0.05 (Kruskal–Wallis followed by Dunn's multiple comparisons post-hoc test). Significance is shown compared to sham control. (D) TUNEL assay to detect dying cells at 4 hpl, 1 dpl and 2 dpl. Images are maximum intensity projections of transverse sections. D, dorsal; V, ventral. In the overview images, a white asterisk indicates the central canal. Scale bars: 5 µm in insets; 100 µm in overviews. (E) TUNEL$^+$ cells were significantly increased at 1 dpl compared to sham controls. Data are mean±s.e.m. Numbers in the plots represent experimental animals. **P≤0.01 (Kruskal–Wallis test followed by Dunn's multiple comparisons post-hoc test). Significance is shown compared to sham control. (F) The number of *mbp*:eGFP$^+$/TUNEL$^+$ cells between sham control and lesioned group remains very low at all investigated time-points. Data are mean±s.e.m. Numbers in the plots indicate the number of experimental animals. (G) Cell loss occurs in a spatially confined manner, spanning a 700 µm zone [±350 µm along the rostrocaudal (RC) axis] around the transection site – referred to as the lesion site.

increased already at 7 dpl and remained significantly increased at 42 dpl (Fig. 3B,C). To determine whether tissue architecture is restored and ventricle size regresses long term, we analysed fish at 1 year post lesion (ypl). Intriguingly, the central canal at the lesion site remained enlarged, when compared with sites distal to the transected area (Fig. 3D,E). Taken together, these data suggest that,

Development (2020) 147, dev193946. doi:10.1242/dev.193946

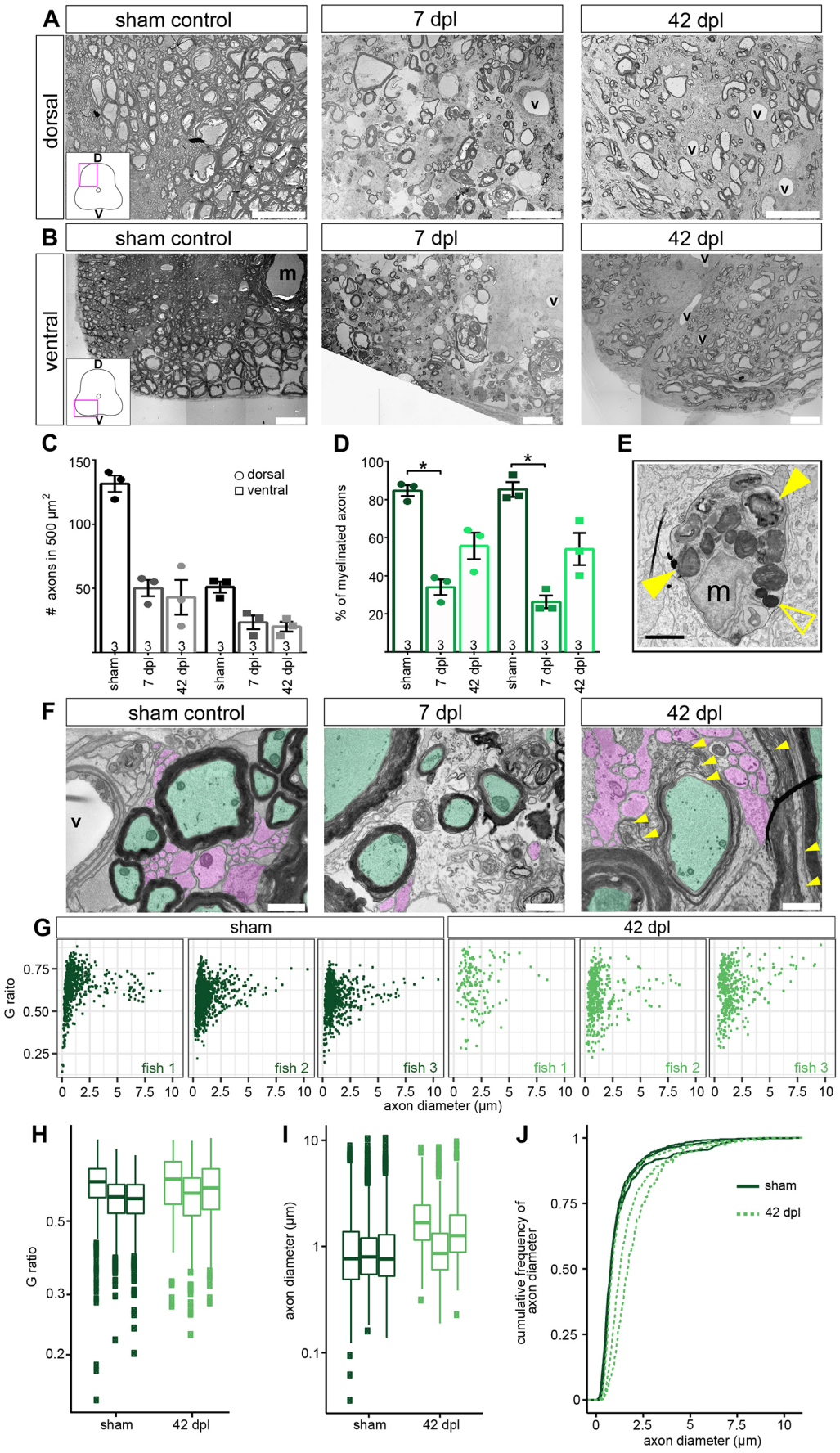

Fig. 2. SCI results in axonal and myelin sheath loss, and different myelin patterns between individual fish. (A,B) Myelinated and non-myelinated axons are decreased after SCI. Overview images are TEM images of transverse sections. D, dorsal; V, ventral (m, Mauthner axon; v, blood vessel). Scale bars: 20 µm. (C) Quantification of axons in a 500 µm^2 area after SCI. Data are mean±s.e.m. Numbers in the plots indicate the number of experimental animals. (D) Percentage of myelinated axons after SCI. Data are mean±s.e.m. Numbers in the plots indicate the number of experimental animals. *P≤0.05 (Kruskal–Wallis followed by Dunn's multiple comparisons post-hoc test). Significance is shown compared to sham control. (E) Macrophage/microglia engulfing myelin debris (filled yellow arrowheads) and lipid droplets (empty yellow arrowhead). Scale bar: 1 µm. (F) SCI results in thinner/still forming myelin sheaths after (re-)myelination. Axons are pseudo-coloured (green, myelinated; magenta, non-myelinated; yellow arrowheads, newly formed myelin sheaths; v, blood vessel). Images are TEM close-ups of transverse sections. Scale bars: 1 µm. (G) G-ratio over axon diameter for all individual fish investigated from the sham control and the 42 dpl group. Each dot represents an axon. (H) G-ratio analysis of all individual fish investigated from the sham control (dark green) and 42 dpl group (light green). Data are presented as box-and-whisker plots, each box presents one of the individual fish shown in G (150-1524 axons were measured per fish). (I) Axon diameter of all individual fish investigated from sham control and 42 dpl group. Data are presented as in H. (J) Cumulative frequency of axon diameter of myelinated axons in sham controls and at 42 dpl.

Development (2020) 147, dev193946. doi:10.1242/dev.193946

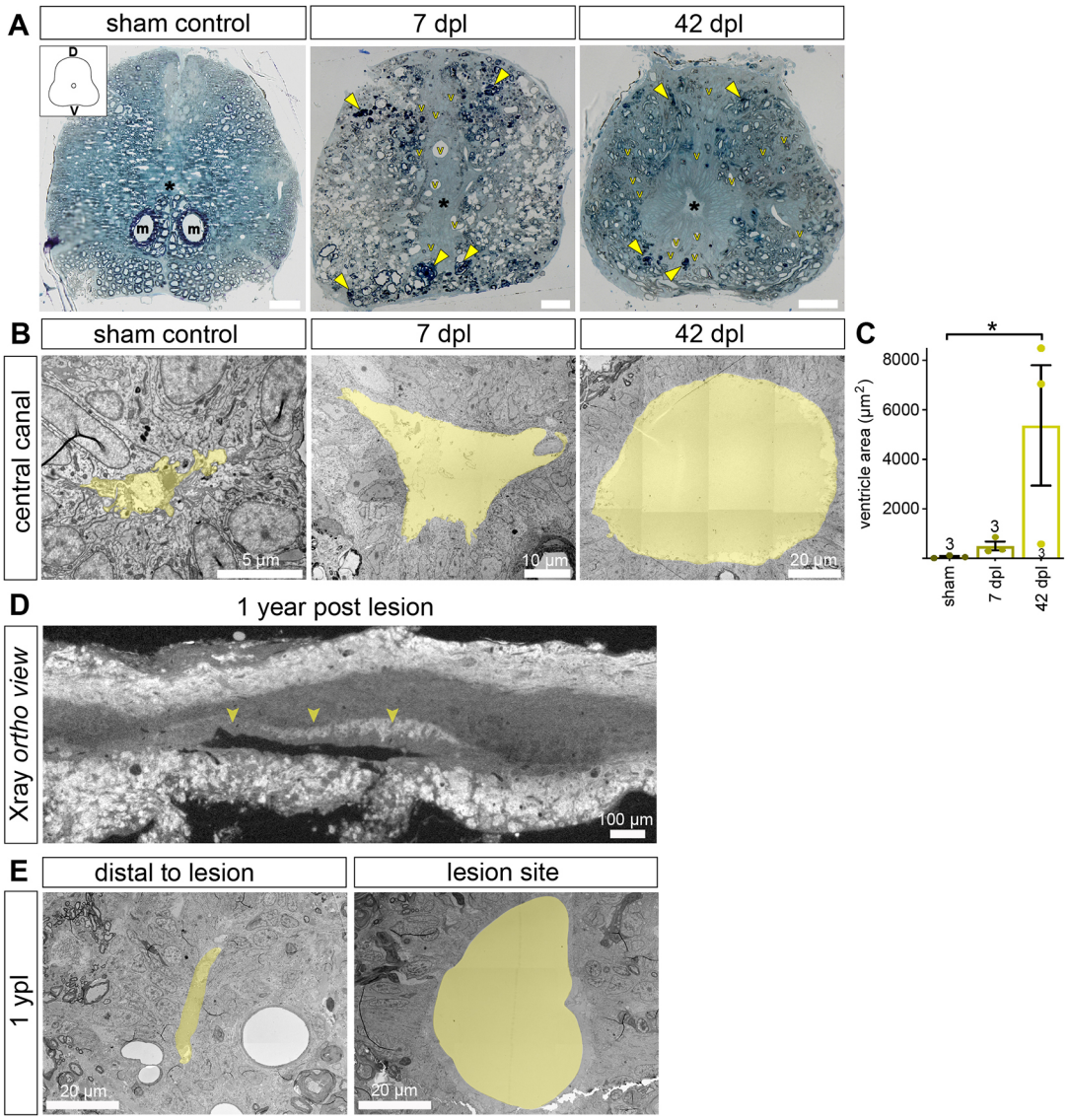

Fig. 3. SCI results in altered tissue architecture close to the transection site that persists at 1 ypl. (A) Semi-thin transverse spinal cord sections stained with Toluidine Blue/borax to visualize membranes. Sections at 7 dpl and 42 dpl come from the rostral part of the lesion site, and ∼50 µm from the transection site. In the overview images, a black asterisk indicates the central canal (m, Mauthner axon; v, blood vessel). D, dorsal; V, ventral. At 7 dpl, myelin debris is indicated by yellow arrowheads. At 42 dpl, tissue integrity is largely restored, yet tissue architecture does not return to its pre-injury characteristics. Vessels and ventricular area remain markedly increased. Scale bars: 50 µm. (B,C) SCI results in an increase in the area of the central canal that persists at 42 dpl. Images are TEM close-ups of transverse spinal cord sections. The central canal is pseudo-coloured (yellow). Data are mean±s.e.m. Numbers in the plots indicate the number of experimental animals.*$P \leq 0.05$ (Kruskal–Wallis followed by Dunn's multiple comparisons post-hoc test). Significance is shown compared to sham control. (D) X-ray microtomography (XµCT) to identify the lesion site at 1 ypl. Shown is an optical section of the orthogonal view after the scan was reconstructed as a TIFF stack. The position of the lesion site (including the transection site) was determined based on the size of the ventricle along the anterior-posterior axis of the spinal cord. (E) The area of the central canal at the lesion site remains increased at 1 ypl when compared with sites distal to the transected area (n=2). Images are TEM close-ups of transverse spinal cord sections. The central canal is pseudo-coloured (yellow).

although swimming activity recovers by 42 dpl (Becker et al., 2004), anatomical and myelination features of the regenerated zebrafish spinal cord do not fully return to pre-injury levels.

OPCs persist through the primary insult and become reactive

To monitor OPC-specific responses after SCI in zebrafish, we examined the Tg(*olig2*:eGFP) line, in which eGFP is driven by the *olig2* promoter (Shin et al., 2003) (Fig. 4A). In the adult zebrafish spinal cord, *olig2*:eGFP labels OPCs in the parenchyma and a subset of ventricular radial glia that can be distinguished from parenchymal OPCs based on their size, morphology and expression of radial glia markers (Fig. S3) (Kroehne et al., 2017). We found that the number of parenchymal *olig2*:eGFP$^+$ cells was transiently reduced at 7 dpl compared to sham controls, but returned to pre-injury levels by 42 dpl (Fig. 4B). Interestingly, however, OPCs reacted rapidly after the lesion, as indicated by marked changes in their cellular morphology. Under physiological conditions, the majority of parenchymal *olig2*:eGFP$^+$ cells displayed a round cell body with thin bipolar processes, thereafter referred to as 'non-reactive' (Fig. 4A, insets and enlargements). In contrast, at 3 dpl, we observed that 92.5±1.6% of parenchymal *olig2*:eGFP$^+$ cells were activated, as indicated by a marked increase in their cell size and the extension of long multi-branched processes (Fig. 4A, insets and enlargements; Fig. 4C), thereafter referred to as 'reactive'. The percentage of reactive parenchymal *olig2*:eGFP$^+$ cells remained

Development (2020) 147, dev193946. doi:10.1242/dev.193946

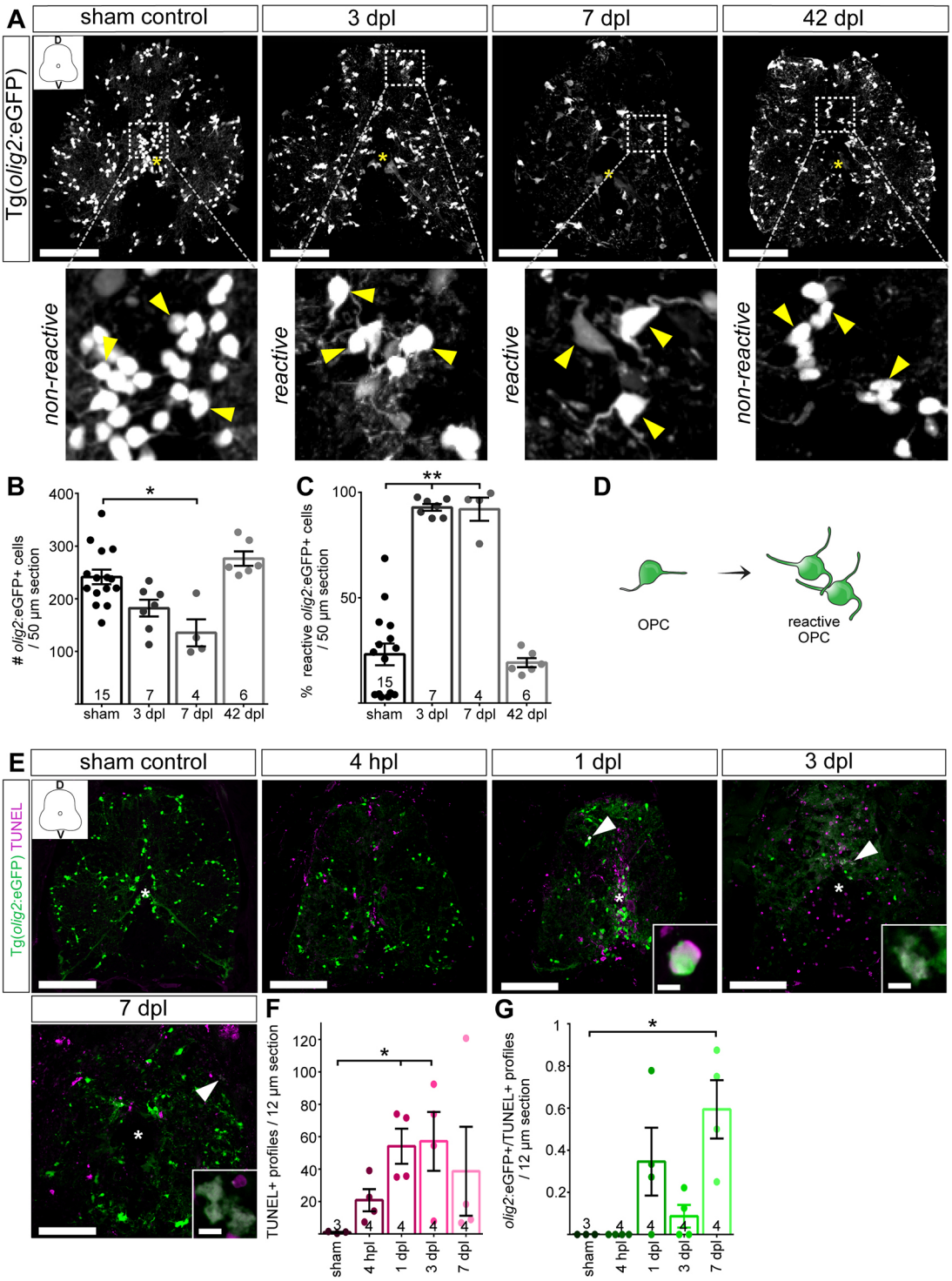

Fig. 4. See next page for legend.

significantly increased at 7 dpl, while the morphology of reactive OPCs returned to sham control levels by 42 dpl (Fig. 4A, insets and enlargements; Fig. 4C). Hence, these data indicate that zebrafish OPCs are a highly dynamic population that readily senses and responds to injury while maintaining its pool (Fig. 4D).

To exclude the possibility that (1) OPCs are dying at very early time-points after the injury and (2) the transient, yet significant, reduction of OPCs at 7 dpl is due to cell death, we performed the TUNEL assay and monitored cell death at 4 hpl, 1 dpl, 3 dpl and 7 dpl (Fig. 4E). Consistent with our analysis in the Tg(*mbp*:eGFP) line (see Fig. 1E), we readily detected an increase in the number of dying cells over baseline levels early after SCI (Fig. 4F). Interestingly, this transient increase was accompanied by a significant increase of immune cells at 7 dpl, as indicated by staining with the pan-leukocyte marker L-plastin, that could contribute to the rapid clearance of dying cells (Fig. S4). In contrast, the number of *olig2*:eGFP^{+}/TUNEL^{+} cells remained very low, with less than one cell per section at all investigated time-points, although a significant increase over baseline

Development (2020) 147, dev193946. doi:10.1242/dev.193946

Fig. 4. OPCs undergo distinct morphological changes after spinal cord transection. (A) The morphology of parenchymal OPCs (enlargements, yellow arrowheads) changes as cells enter a 'reactive' state immediately after SCI. Changes are indicated by marked increase in their cell size and the extension of long multi-branched processes. Activation features persist at 7 dpl and return to control levels at 42 dpl. Images are maximum intensity projections of transverse sections. D, dorsal; V, ventral. In the overview images, a yellow asterisk indicates the central canal. Scale bars: 100 µm. (B) Stereological quantification of parenchymal *olig2*:eGFP$^+$ cells 700 µm around the transection site shows a significant reduction in OPCs at 7 dpl, compared to sham controls. Data are mean±s.e.m. Numbers in the plots indicate the number of experimental animals. *P≤0.05 (Kruskal–Wallis test followed by Dunn's multiple comparisons post-hoc test). Significance is shown compared to sham control. (C) At 3 and 7 dpl, the percentage of reactive cells is significantly increased between lesioned and sham control animals. Data are mean±s.e.m. Numbers in the plots indicate the number of experimental animals. **P≤0.01 (Kruskal–Wallis test followed by Dunn's multiple comparisons post-hoc test). Significance is shown compared to sham control. (D) Schematic representation of morphological changes indicating activation features of reactive OPCs after SCI. (E) TUNEL assay to detect dying cells at 4 hpl, 1 dpl, 3 dpl and 7 dpl. Images are maximum intensity projections of transverse sections. D, dorsal; V, ventral. In the overview images, a white asterisk indicates the central canal. Scale bars: 5 µm in insets; 100 µm in overviews. (F) TUNEL$^+$ cells were significantly increased at 1 and 3 dpl, compared to sham controls. Data are mean±s.e.m. Numbers in the plots indicate the number of experimental animals. *P≤0.05 (Kruskal–Wallis test followed by Dunn's multiple comparisons post-hoc test). Significance is shown compared to sham control. (G) A significant increase in the number of dying *olig2*:eGFP$^+$/TUNEL$^+$ cells was detected at 7 dpl. However, the number of *olig2*:eGFP$^+$/TUNEL$^+$ cells remains below 1 cell per section at all investigated time-points. Data are mean±s.e.m. Numbers in the plots indicate the number of experimental animals. *P≤0.05 (Kruskal–Wallis test followed by Dunn's multiple comparisons post-hoc test). Significance is shown compared to sham control.

levels was detectable at 7 dpl (Fig. 4G). However, given the total number of OPCs at 7 dpl, this corresponds to less than 2% of the total OPC population. Taken together, these data are consistent with a scenario in which adult zebrafish OPCs vastly survive the primary insult and do not undergo cell death after lesion.

OPCs react to SCI by increasing proliferation

As the number of *olig2*:eGFP$^+$ OPCs and *mbp*:eGFP$^+$ oligodendrocytes cells returned to control levels by 42 dpl, we examined the induction of acute OPC proliferation after SCI. To detect cycling cells and determine spatial changes in cell proliferation, we used an antibody to PCNA that labels proliferating cells (Fig. 5A) and quantified the number of *olig2*:eGFP$^+$/PCNA$^+$ cells starting from 700 µm rostral to 700 µm caudal to the lesion site. We detected a significant increase in the number of parenchymal *olig2*:eGFP$^+$/PCNA$^+$ cells within a 700 µm zone around the transection site (±350 µm along the RC axis) compared to sham controls, in which proliferation levels were lower (Fig. 5B). This suggested an immediate proliferative reaction of OPCs in the lesion site, in response to the acute insult.

As indicated previously, the majority of the *olig2*:eGFP$^+$ cells detectable at 7 dpl displayed a reactive morphology. We therefore sought to determine whether proliferation is a property linked exclusively to reactive OPCs, or whether non-reactive cells are as likely to proliferate as reactive cells. As sham controls have a much higher proportion of non-reactive OPCs, we examined proliferating *olig2*:eGFP$^+$/PCNA$^+$ cells in the sham control group. We found *olig2*:eGFP$^+$/PCNA$^+$ cells in both populations of non-reactive and reactive OPCs (Fig. 5C). This suggests that proliferation is not specifically linked to features of cell activation, and that the morphological changes observed in reactive cells might serve functions other than exclusively proliferation (Fig. 5E). For example, reactive cells might not only proliferate to replenish the population, but also migrate in from outside the 700 µm zone, such that their morphological changes might reflect migratory cytoskeletal rearrangements. In order to investigate such a scenario, we examined the spatial distribution of OPCs by quantifying the number of *olig2*:eGFP$^+$ cells along the RC axis (Fig. 5D). At 7 dpl, the number of *olig2*:eGFP$^+$ cells was found to be unaltered along the RC axis, suggesting that OPC total numbers are not altered by immigration of distal cells.

Finally, to examine the cellular dynamics of the OPC population, we monitored OPC turnover at the whole-tissue level. To examine whether acute proliferation contributes to the re-establishment of the OPC population after injury, we injected EdU to label proliferating cells in the S-phase of the cell cycle, and examined the whole-mount spinal cord using tissue clearing (Susaki et al., 2014) (Fig. 5F,G). As expected, we observed that in the unlesioned spinal cord of sham controls, proliferation levels were very low, with parenchymal *olig2*:eGFP$^+$/EdU$^+$ cells representing less than 1% of the total *olig2*:eGFP$^+$ population in the parenchyma (Fig. 5H, sham control). In contrast, at 14 dpl, the number of EdU$^+$ cells was markedly increased, both in the parenchyma and around the ventricular central canal (Fig. 5H, 14 dpl). Parenchymal *olig2*:eGFP$^+$ cells significantly increased proliferation compared to sham controls, with almost 10% of the total population retaining EdU (Fig. 5I). This indicates that, in the regenerating zebrafish spinal cord, OPCs are able to replenish their population after injury by increasing proliferation.

SCI induces *de novo* generation of *mbp*:eGFP$^+$ oligodendrocytes

Our data suggest that less than 2% of OPCs are dying at 7 dpl, and that the population of *mbp*:GFP$^+$ oligodendrocytes is re-established at 14 dpl. Therefore, a possible scenario might be that the transient decrease of OPCs at 7 dpl is due to their differentiation into oligodendrocytes. Indeed, immunostaining against Claudin K (which labels mature oligodendrocytes and myelin sheaths) and Neurofilament (which labels axonal filaments) in Tg(*olig2*:eGFP) fish at 7 dpl, revealed that some reactive OPCs are expressing Claudin K, while being closely apposed to axons, indicating their differentiation into pre-myelinating oligodendrocytes (Fig. 6A).

Next, we analysed the generation of new oligodendrocytes after SCI in the Tg(*mbp*:eGFP) line, after injection of EdU (Fig. 6B). We found that, at 14 dpl, the number of newly generated *mbp*:eGFP$^+$/EdU$^+$ cells was significantly higher when compared with sham controls (Fig. 6C,D). This suggests that, in the regenerating adult zebrafish spinal cord, OPCs differentiate into mature oligodendrocytes, and new *mbp*:eGFP$^+$ oligodendrocytes are generated (Fig. 6E).

Reactive OPCs differentially express genes related to oligodendrocyte differentiation after SCI

The molecular signature associated with OPC responses in a regenerative context is currently unknown. Because the morphology of OPCs has been previously described to define their maturation state (Huang et al., 2011), we hypothesized that reactive OPCs might become pre-myelinating, and thus eventually contribute to (re-)myelination of spared and regrown axonal segments.

To determine the molecular signature of the initiation of myelination, we transcriptionally profiled OPCs isolated from the zebrafish spinal cord at 7 dpl, when OPC activation features are markedly detectable and reactive proliferation is at its peak. As SCI results in a spatially restricted damage and cellular responses are strictly confined within 700 µm around the transection site, we dissociated, FAC-sorted and analysed the transcriptome of *olig2*:eGFP$^+$ OPCs from ∼0.5 mm of spinal cord tissue (Fig. 7A; Fig. S5, Fig. S6A-C). Comparing lesioned (reactive OPCs) with sham

Development (2020) 147, dev193946. doi:10.1242/dev.193946

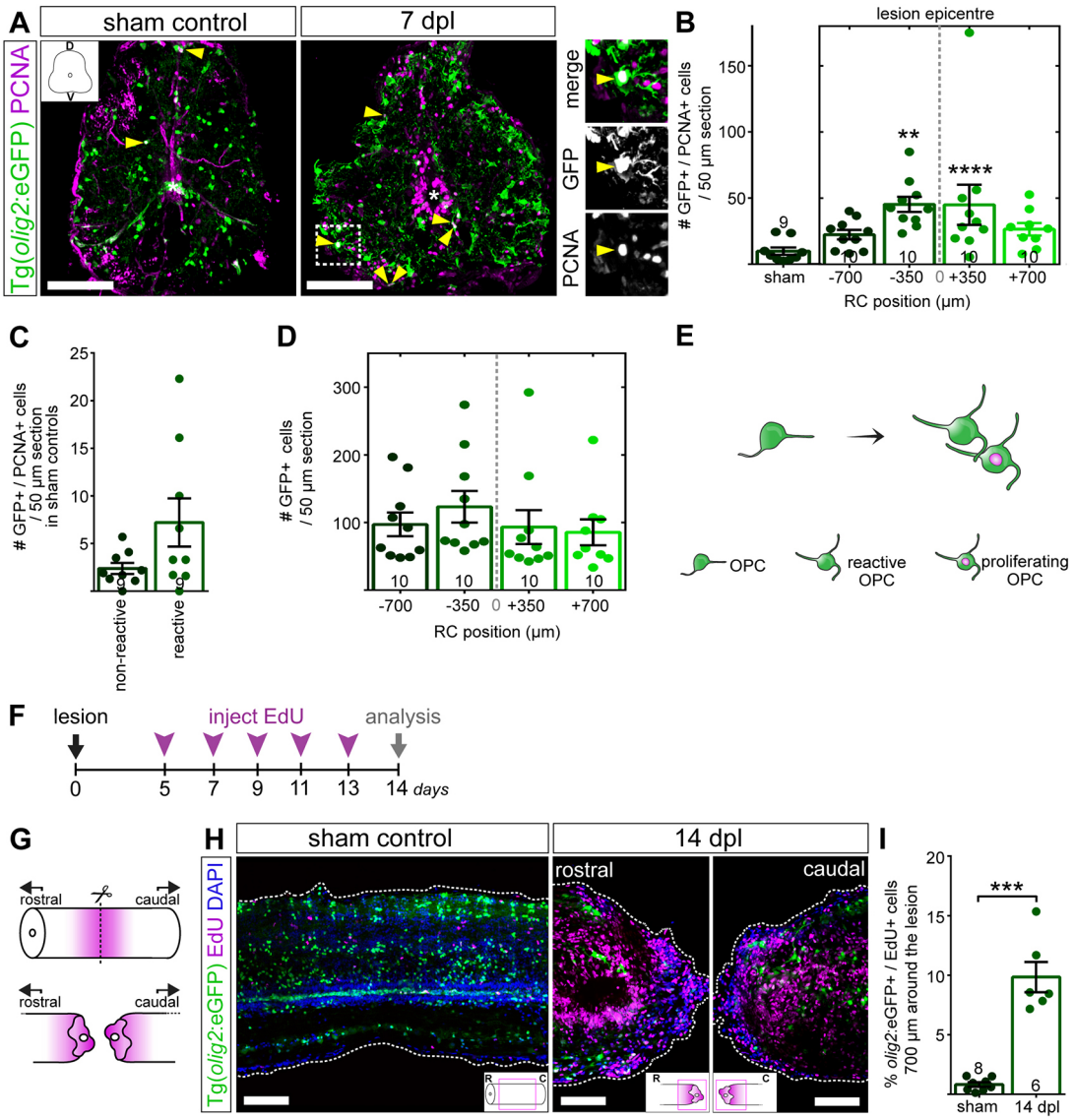

Fig. 5. OPCs increase proliferation after SCI. (A) At 7 dpl, proliferating *olig2*:eGFP$^+$/PCNA$^+$ OPCs can be detected both in the parenchyma and the ventricle (overview/inset, yellow arrowheads). Images are maximum intensity projections of transverse sections. D, dorsal; V, ventral. In the overview images, a white asterisk indicates the central canal. Scale bars: 100 µm. (B) Stereological quantification of parenchymal *olig2*:eGFP$^+$/PCNA$^+$ cells 700 µm around the transection site shows a significant increase in proliferating OPCs at 7 dpl, compared to sham controls. Data are mean±s.e.m. Numbers in the plots indicate the number of experimental animals. ****$P\leq0.0001$; **$P\leq0.01$ (Kruskal–Wallis test followed by Dunn's multiple comparisons post-hoc test). Significance is shown compared to sham control. (C) Stereological quantification of parenchymal *olig2*:eGFP$^+$/PCNA$^+$ cells 700 µm around the transection site in sham controls shows that both non-reactive and reactive OPCs proliferate. (D) Stereological quantification of parenchymal *olig2*:eGFP$^+$ cells 1400 µm around the transection site at 7 dpl shows no significant difference in the GFP$^+$ cells along the RC axis (Kruskal–Wallis test followed by Dunn's multiple comparisons post-hoc test). (E) Schematic representation of OPCs becoming reactive immediately after lesion and proliferating. (F) Timeline of EdU labelling experiment to monitor generation of new OPCs. (G) Strategy to image and analyse OPC proliferation in whole-mount tissue after SCI and tissue clearance. (H) Optical section of whole-mount zebrafish spinal cord of transgenic Tg(*olig2*:eGFP) fish after CUBIC-based tissue clearance. At 14 dpl, the size of the ventricle is markedly increased (see also Fig. 4), while proliferation of both parenchymal and ventricular cells is upregulated. Scale bars: 100 µm. (I) Quantification of the percentage of *olig2*:eGFP$^+$/EdU$^+$ parenchymal OPCs 700 µm around the transection site after 3D-reconstruction in Imaris shows a significant increase in the percentage of newly generated OPCs at 14 dpl, compared to sham controls. Data are mean±s.e.m. Numbers in the plots indicate the number of experimental animals. ***$P\leq0.001$ (Mann–Whitney test). Significance is shown compared to sham control.

control (non-reactive) samples, we identified a total of 1755 differentially expressed genes (DEGs). Of these, 1124 genes were upregulated and 631 genes were downregulated. Gene ontology (GO) analysis resulted in the classification of DEGs into six major categories, including developmental, growth and metabolic processes (Fig. 7B). As it was initially hypothesized that reactive OPCs might contribute to (re-)myelination, the DEGs were analysed based on their functional annotations, using GO terms related to the process of myelination. Reactive OPCs upregulated a plethora of genes involved in migration, cell adhesion and cytoskeletal remodelling, as well as genes related to cell cycle and differentiation, lipid metabolism, protein and vesicular transport. Importantly, reactive OPCs upregulated genes expressed in mature oligodendrocytes and related to compact myelin formation (Fig. 7C,D). Interestingly, the upregulation of differentiation-related genes in reactive OPCs was also concomitant with the

Development (2020) 147, dev193946. doi:10.1242/dev.193946

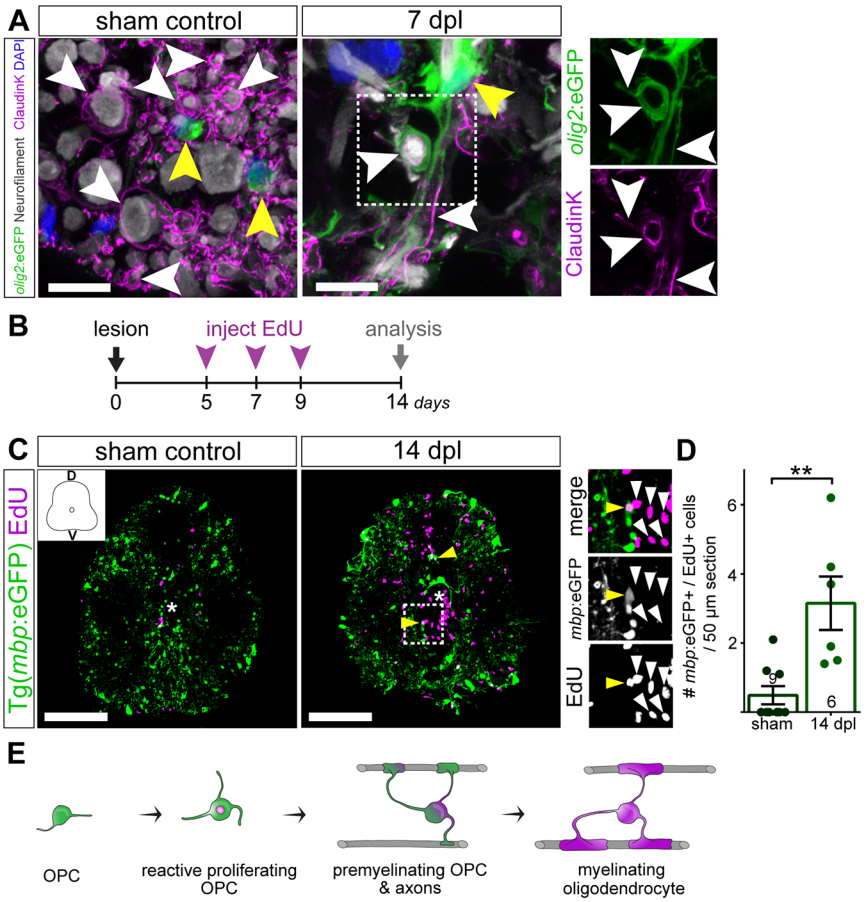

Fig. 6. Generation of new oligodendrocytes after SCI. (A) Immunostaining for Claudin K (magenta; labelling oligodendrocytes and myelin sheaths) and Neurofilament (grey; labelling axonal filaments) in Tg(*olig2*:eGFP) sham and 7 dpl fish. In sham controls, OPCs are small and round (sham control, yellow arrowheads) and myelin sheaths enwrap axons in a highly organized manner. SCI results in marked axonal loss and in OPCs becoming reactive (7 dpl, yellow arrowheads). At the same time-point, a proportion of reactive OPCs which is in contact with axons are Claudin K^{+}, indicative of their differentiation into myelinating oligodendrocytes. Images are maximum intensity projections of transverse sections. Scale bars: 10 µm. (B) Timeline of EdU labelling experiment to monitor newly generated oligodendrocytes. (C) SCI causes an increase of newly generated cells (insets, white arrowheads) 700 µm around the lesion site from 5 to 14 dpl. Newly generated oligodendrocytes (*mbp*:eGFP^{+}/EdU^{+}) can be detected in all areas of the lesioned spinal cord (overview/insets, yellow arrowheads). Images shown are maximum intensity projections of transverse sections. D, dorsal; V, ventral. In the overview images, a white asterisk indicates the central canal. Scale bars: 100 µm. (D) Stereological quantification of *mbp*:eGFP^{+}/EdU^{+} cells 700 µm around the lesion site shows a significant increase in the number of newly generated oligodendrocytes at 14 dpl compared to sham controls. Data are mean±s.e.m. Numbers in the plots indicate the number of experimental animals. $^{**}P \leq 0.01$ (Mann–Whitney test). Significance is shown compared to sham control. (E) Schematic representation of OPC myelination at 7 dpl and generation of oligodendrocytes by 14 dpl. A proportion of reactive OPCs becomes pre-myelinating, providing fast myelination of spared axons.

upregulation of several genes associated with immune system function, such as *tnfrsf11a*, *cxcl14*, *il4r.1* and *stat6* (Fig. S7). Intriguingly, single-cell RNAseq showed that reactive OPCs fall into distinct clusters (Fig. S6D,E), suggesting functional heterogeneity within the OPC population after SCI.

To verify our RNASeq dataset, we performed fluorescent *in situ* hybridization in Tg(*olig2*:eGFP) fish at 7 dpl. We selected four genes (*apoeb*, *ctgfa*, *sema3c* and *tnc*) based on their high counts. Quantification of the number of parenchymal OPCs expressing the respective genes confirmed their upregulation after SCI, validating our transcriptome data (Fig. 8). Taken together, these data suggest that, in the adult zebrafish spinal cord at 7 dpl, OPCs initiate transcriptional programmes related to differentiation, membrane formation and, thus, oligodendrocyte maturation.

DISCUSSION

Cellular origin of myelin sheaths after SCI

In this study, we provide previously unreported insights into oligodendroglial lineage cell biology after SCI in a regenerating vertebrate. Using a spinal cord transection paradigm, we show that the initial cellular processes orchestrating injury responses in adult zebrafish resemble those seen in mammals (Papastefanaki and Matsas, 2015). We find that >60% of oligodendrocytes are lost within 7 dpl. Intriguingly, within the same time-frame we did not detect significant death of oligodendrocytes. This raises the possibility that, in the zebrafish spinal cord, oligodendrocytes are injury resistant. However, owing to technical limitations we cannot draw definite conclusions. These include the possibility that *mbp*:eGFP^{+}/TUNEL^{+} oligodendrocytes have been missed due to (1) GFP expression downregulation in the Tg(*mbp*:eGFP) reporter line and/or (2) the segregation of membrane-tethered signal occurring during myelin formation by oligodendrocytes (Aggarwal et al., 2011). Similarly, we cannot exclude the possibility that pre-existing oligodendrocytes might de-differentiate to become (re-)myelinating OPCs, owing to lack of a functional Cre-based genetic lineage tracing. A relatively weak expression level of Cre is required in an inducible CreER^{T2} system in order to avoid unconditional recombination (Kroehne et al., 2011). Moreover, as OPC differentiation is induced by tamoxifen

Development (2020) 147, dev193946. doi:10.1242/dev.193946

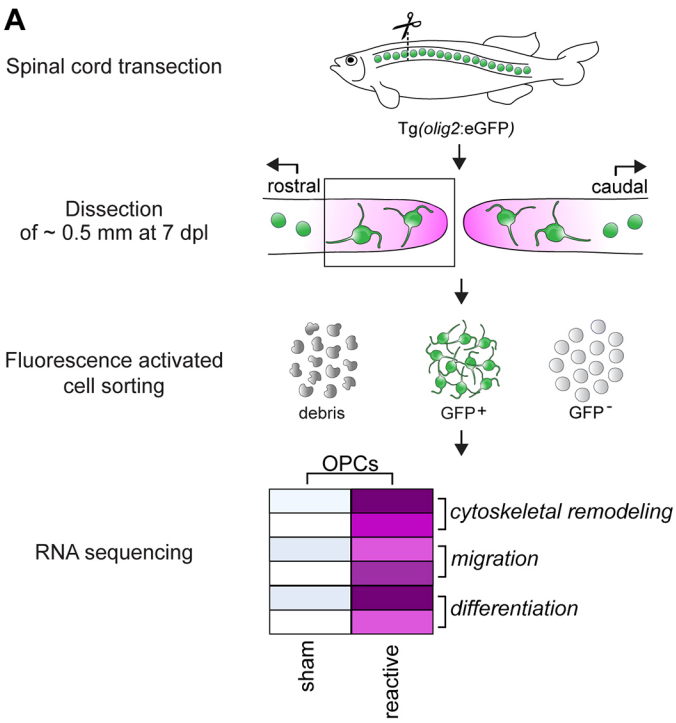

B GO analysis on DEGs in reactive OPCs

Enriched Biological Function	Number of genes	*P* value
developmental process	321	8.4×10^{-5}
cellular process	916	1.0×10^{-4}
growth	46	5.5×10^{-4}
cellular component or biogenesis	268	7.3×10^{-4}
metabolic process	614	2.5×10^{-3}
multicellar organismal process	313	5.7×10^{-2}

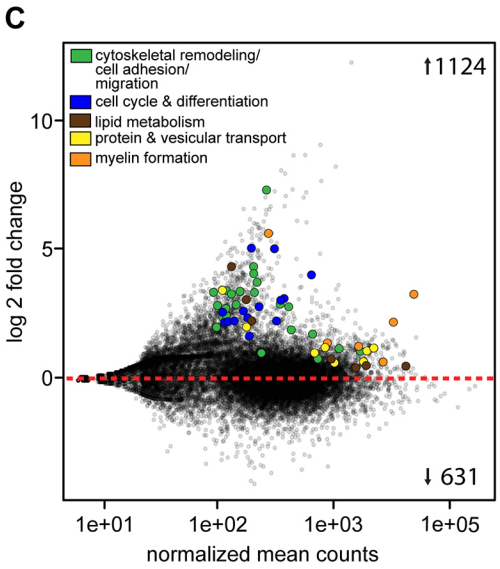

D

cytoskeletal remodeling & cell adhesion & migration	*nrcama, sdc4, neo1a, cd99, bcam, ctgfa, itga6a, itgb6, tnc, gli1, dnah2, dnah12, kif26ab, pls3, slit3, sdc4, met, smarca4a, cdh2, lama4, sema3fa, sema3c, masp1, nrp2b*
cell cycle & differentiation	*chek1, cdkn1cb, gmnn, wnt4b, elk3, isl1, sox19, mturn, metrn, neurod1, neurod4, notch3, ppp2r3a*
lipid metabolism	*elovl1b, npc2, echdc2, plcxd3, pafah1b1a, smpd3, degs1*
protein transport & vesicular transport	*tram2, gdi, sec61a1, sec61b, clta, vamp5, stx7l*
myelin formation	*mbpb, apoeb, tuba813*

Fig. 7. Reactive OPCs upregulate genes involved in differentiation and myelin formation. (A) Experimental pipeline to investigate the transcriptional profile of reactive OPCs with RNAseq. The spinal cord of adult zebrafish is transected. At 7 dpl, ~0.5 mm of spinal cord tissue (rostral part) is dissected. For sham control fish, a ~0.5 mm tissue is dissected at the same area of the spinal cord along the rostral to caudal axis of the fish. A calcein AM dye step is used to stain for viable cells. *olig2*GFP^{+}/calcein^{+} OPCs are FAC sorted and processed for the preparation of an RNAseq library. DEGs between lesioned (reactive OPCs) and sham control (non-reactive) groups are analysed. (B) Gene ontology (GO) analysis on DEGs in reactive versus non-reactive OPCs at 7 dpl revealed enrichment for processes involved in development, growth, biogenesis and metabolism. (C) Plot of mean normalized counts over fold-change in reactive versus non-reactive OPCs of DEGs at 7 dpl. Each dot represents a gene. (D) Genes were selected based on their functional annotation to processes involved in myelination.

Development (2020) 147, dev193946. doi:10.1242/dev.193946

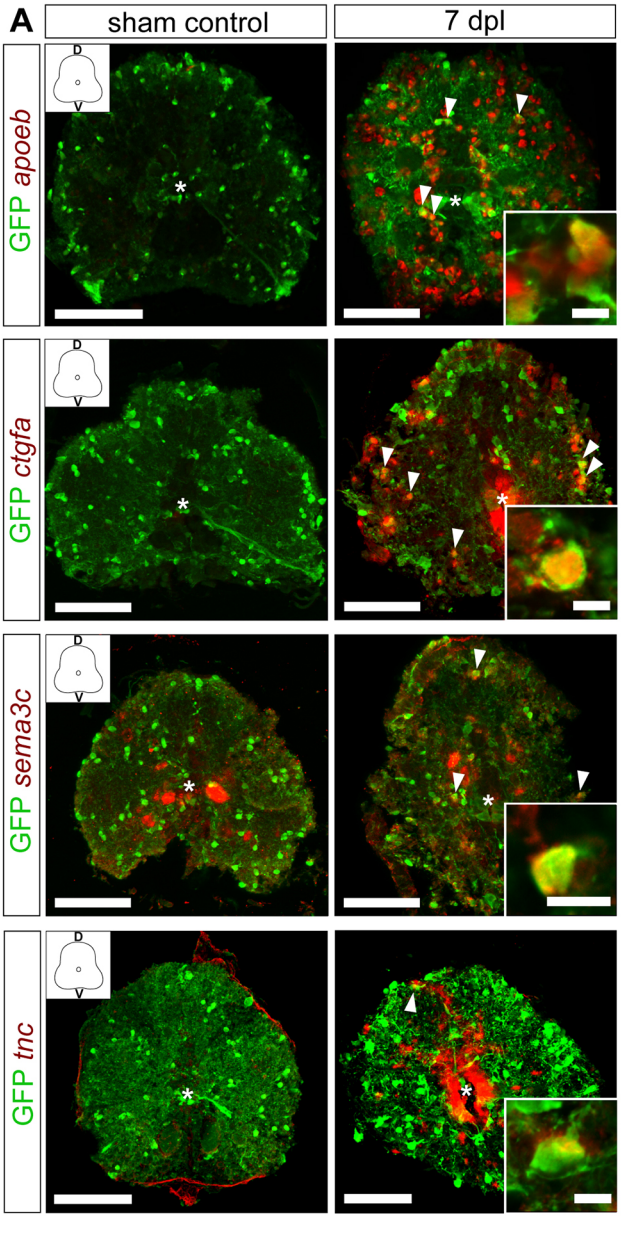

Fig. 8. Validation of RNAseq candidate genes with fluorescent *in situ* hybridization. (A) Fluorescent *in situ* hybridization for *apoeb*, *ctgfa*, *sema3c* and *tnc* in Tg(*olig2*:eGFP) fish. SCI results in gene expression upregulation (red) in the spinal cord parenchyma (*ctgfa*, *tnc*, *sema3c* and *apoeb*) and in the central canal (*ctgfa* and *tnc*) at 7 dpl. Sections were co-stained using anti-GFP antibody. Overview images are maximum intensity projections of transverse sections. D, dorsal; V, ventral. In the overview images, a white asterisk indicates the central canal. Scale bars: 10 µm in insets; 100 µm in overviews. (B) Quantification of mRNA^{+}/GFP^{+} cells in 50 µm sections, 350 µm rostral to the lesion site shows a significant increase in the number of OPCs upregulating the respective gene at 7 dpl, compared to sham controls. Data are mean±s.e.m. Numbers in the plots indicate the number of sections counted. Number of experimental animals were as follows: six sham control and six lesioned for *apoeb*, *ctgfa* and *tnc*; eight sham and eight lesioned for *sema3c*. $^{**}P\leq0.01$; $^{***}P\leq0.001$; $^{****}P<0.0001$ (Mann–Whitney test). Significance is shown compared to sham control.

(Gonzalez et al., 2016), this would interfere with the usage of the CreER^{T2} system and its tamoxifen inducer. In the absence of such a marking technique, it is inherently difficult to distinguish between a possible contribution from spared oligodendrocytes that are able to re-myelinate (Duncan et al., 2018b; Yeung et al., 2019; Bacmeister et al., 2020), and spared oligodendrocytes that de-differentiated and initiated secondary (re-)myelination.

Similar to what has been shown in a mouse model of demyelination (Romanelli et al., 2016), at the ultrastructural level the primary impact causes a clear disruption of tissue architecture, axonal and myelin sheath loss, accompanied by a pronounced inflammatory response of activated macrophage/microglia. This is in accordance with studies in mammals, where the initial injury affects blood vessels, including blood-brain barrier (BBB) disruption, leading to the immediate infiltration of peripherally derived immune cells to the injury site (Habgood et al., 2007). Surprisingly, the data acquired in this study suggest that, in contrast to mammals, zebrafish oligodendrocyte numbers return to pre-injury levels by 42 dpl, the time-point of functional recovery (Becker et al., 1997). Interestingly, by this time, total axon number and percentage of myelinated axons, have not returned to pre-injury levels. In addition, the majority of myelinated axons is insulated by myelin sheaths of lower compaction that resemble newly forming myelin sheaths during development (Bunge et al., 1961). Taken together, our data suggest that in the adult zebrafish spinal cord, functional recovery coincides with partially recovered axonal profiles and myelination. This is consistent with previously published data in zebrafish (Kuscha et al., 2012) and other vertebrates, where thinner myelin sheaths were shown to stabilize axonal survival (Duncan et al., 2017) and ensure proper signal conduction (Smith et al., 1979). Our results suggest that, at the point of functional restoration, (re-)myelination is not complete, and argue in favour of the possibility that neuronal activity (Mensch et al., 2015) and/or individual axon subtypes (Almeida et al., 2011; Koudelka et al., 2016) actively regulate myelin sheath formation and remodelling (Auer et al., 2018). This is further supported by the observed increase in axon diameter of

Development (2020) 147, dev193946. doi:10.1242/dev.193946

myelinated axons at 42 dpl, as, similarly, axon calibre size has been previously shown to trigger myelination (Goebbels et al., 2017). Accordingly, a longer recovery and myelin refinement period might be required to monitor the extent of complete (re-)myelination after SCI in adult zebrafish. This is particularly interesting given the restricted time-window in which new myelin sheaths are formed by individual oligodendrocytes during development (Czopka et al., 2013). Full-thickness myelin sheaths have been observed to form in the spinal cord of larvae, in the optic nerve of juvenile zebrafish (Münzel et al., 2014; Karttunen et al., 2017) and in the spinal cord of adult mice (Powers et al., 2013). Future studies need to examine whether (1) the number of myelin sheaths per oligodendrocyte and/or (2) the myelin sheath length is altered, compared to pre-injury levels. Interestingly, using a larval zebrafish model of demyelination, Neely et al. recently showed that the myelination pattern of newly generated oligodendrocytes involves more myelin sheaths as compared to before demyelination, and shorter average sheath length that may, however, grow over time (Neely et al., 2020 preprint). These data challenge the notion that functional repair requires complete re-myelination and argue in favour of a necessary threshold of axonal support that subsequently ensures locomotor function, as was recently also reported for a mouse model of SCI (Duncan et al., 2018a).

Injury responses of zebrafish OPCs

An interesting observation of our study is that adult zebrafish OPCs are an apparently robust population that survives SCI. Although a significant reduction of OPC numbers was detectable at 7 dpl, coinciding with a significant increase in TUNEL$^+$ OPCs, this decrease corresponded to less than 2% of the total OPC population. This is an intriguing finding, given the overt loss of OPCs that occurs after CNS injury in mammals, where at 7 dpl, nearly 50% of the NG2$^+$/Olig2$^+$ cells were positive for TUNEL, indicating the vulnerability of mouse NG2$^+$/Olig2$^+$ cells to degeneration (Payne et al., 2013). Our observation is consistent with data from larval zebrafish, in which no *olig2*:GFP$^+$/TUNEL$^+$ cells were detectable after SCI (Ohnmacht et al., 2016). Consistently, at 14 dpl, the number of newly generated oligodendrocytes was significantly increased compared to sham controls. Together, our data suggest that proliferating OPCs need to successfully progress along their lineage to give rise to mature oligodendrocytes, as was recently also observed in a focal demyelinating SCI model in rodents (Foerster et al., 2020 preprint). Interestingly, by 14 dpl, we could detect only three newly generated oligodendrocytes – as a result of progenitor proliferation – as indicated by their retention of EdU (Fig. 6D). However, at the same time-point, we have detected a total of ∼170 oligodendrocytes and, hence, the re-establishment of the oligodendrocyte population (Fig. 1B). We therefore speculate that oligodendrocytes become re-established not only through proliferation, but also directly from reactive OPCs. In this model, a fraction of reactive OPCs might be able to differentiate into oligodendrocytes when demand arises, e.g. by 7 dpl, and without proliferation. This possibility is supported by (1) our observation that myelin-related proteins, such as Claudin K, are expressed in reactive OPCs (Fig. 6A), (2) our RNAseq data showing upregulation of myelin differentiation-related genes in reactive OPCs (Fig. 7) and (3) the number of *mbp*:GFP$^+$/EdU$^+$ cells at 14 dpl (Fig. 6D). In combination with our single-cell analysis, these data are consistent with the existence of functionally distinct subgroups of zebrafish OPCs (Tsata et al., 2019; Marisca et al., 2020) that might respond differently to injury, as previously reported in rodents (Káradóttir et al., 2008).

We find that OPCs enter an activated state and proliferate, despite the concurrent marked inflammation. This points to a coupling between inflammatory response and OPC activation, also observable in the upregulation of several immune system-related genes in reactive OPCs. This is in accordance with previous studies in the regenerating zebrafish brain and spinal cord, where, in contrast to mammals, inflammation is required for the activation of radial glial progenitor cells and axon regeneration (Kyritsis et al., 2012; Tsarouchas et al., 2018). Consistent with such a possibility, the engulfing of myelin/membrane/lipid debris by activated macrophages/microglia at 7 dpl points to the efficient clearance close to the lesion site of degenerating cellular components and/or cellular debris, which might otherwise hinder regeneration (Neumann et al., 2009).

Transcriptional profile of reactive adult zebrafish OPCs

We report the first transcriptome dataset of DEGs in reactive OPCs after transection of the adult zebrafish spinal cord, showing that reactive OPCs systemically express genes related to maturation and myelination. Already by 3 dpl, OPCs have transformed from small, round, bipolar cells to enlarged, highly branched cells, exhibiting changes that, during development, correlate with OPC migration or responses to maturation stimuli and, potentially, their lineage progression to differentiating oligodendrocytes (Ono et al., 2001; Pedraza et al., 2014). Similar morphological changes have also been observed during differentiation of primary adult zebrafish OPCs from the spinal cord during co-culture with human motor neurons (Kroehne et al., 2017). Moreover, *in vitro* analysis of activated OPCs in adult mice has previously revealed an activation-dependent increase in migration and differentiation rates (Moyon et al., 2015). Indeed, our RNAseq data revealed that reactive OPCs upregulate genes related to distinct phases of OPC differentiation, such as migration, cytoskeletal remodelling in axon guidance and membrane formation or transport, all key processes of active myelination. Given the fact that the morphological differences of OPCs are already apparent by 3 dpl, these transcriptional changes presumably have started even earlier. Thus, zebrafish OPCs seem to readily undergo crucial functional changes, unlike mammalian OPCs, where the similar myelination genes are upregulated later and only after OPCs are successfully recruited to the injury site (Huang et al., 2011).

An important factor impeding axonal regeneration in mammals is growth inhibition by the extracellular matrix (ECM), which is also secreted by presumed OPCs (NG2$^+$ cells) (Filous et al., 2014). Recent work in zebrafish has shown that ECM components in the spinal lesion site are permissive and required for axonal regrowth (Wehner et al., 2017), thus creating a regeneration-promoting environment when compared with mammals (Cigliola et al., 2020). Our RNAseq analysis revealed that reactive OPCs upregulate a plethora of genes coding for ECM and ECM-remodelling enzymes, including *ctgfa*, *sema3c* and *tnc*, offering the possibility that OPCs promote regeneration by secreting growth-permissive ECM in the zebrafish lesion site. Together, the genes identified here represent a tantalizing starting point to further test potential targets for the activation of endogenous progenitor cells in non-regenerating environments (Llorens-Bobadilla et al., 2020).

In summary, several lines of evidence obtained in this study support the scenario that in the regenerating zebrafish spinal cord, OPCs contribute to (re-)myelination. First, OPCs enter an activated state and efficiently proliferate despite the marked inflammation. Second, OPCs upregulate several genes involved in oligodendrocyte maturation and differentiation. Third, both activation and increased proliferation result in OPCs becoming pre-myelinating, as well as in formation of new mature oligodendrocytes. Our findings support a model in which the efficient OPC response following SCI may be sufficient to provide the level of (re-)myelination needed, thus

Development (2020) 147, dev193946. doi:10.1242/dev.193946

contributing to the restoration of the injury-induced functional deficits (Fig. 9). Zebrafish OPCs therefore offer an excellent system for studying successful regeneration responses of the oligodendrocyte lineage in a vertebrate of high regenerative capacity, with the potential to developing novel therapeutic strategies for the treatment of spinal cord injuries also in mammals.

MATERIALS AND METHODS

All animal experiments were performed in compliance with animal welfare legislation and were approved by the ethical approval committee of the Regierungspräsidium Dresden, Germany: TVV 53/2015 and TVV 35/2017. All efforts were made to minimize animal suffering and the number of animals used.

Fish maintenance

Fish were kept and bred in our fish facility according to standard methods (Brand et al., 2002). We used Tg(*olig2*:eGFP) (Shin et al., 2003) and Tg(*mbp*:eGFP) zebrafish (Jung et al., 2010).

Spinal cord injury

Adult fish were anaesthetized by immersion in 0.25% w/vol Tricaine (Sigma-Aldrich) and the spinal cord was transected under visual control 5 mm caudal to the brainstem-spinal cord junction, as previously described (Becker et al., 1997). Sham-lesioned fish were treated equally, except that the spinal cord was left intact. Fish were allowed to survive spinal cord injury for up to 42 days. Recovery of swimming activity was confirmed by visual evaluation of all fish that were further processed for the 42 dpl time point.

Electron microscopy

Contrasted ultrathin sections were analysed on a FEI Morgagni D268 (FEI, Eindhoven, The Netherlands) or a Jeol JEM1400 Plus at 80 kV acceleration voltage. The number of axons and G-ratio were manually analysed in Fiji. Images were processed and assembled using Fiji, Adobe Photoshop CS6 and Illustrator CS6. Microsoft Excel was used to process the measured data. For full details, see supplementary Materials and Methods.

TUNEL cell death assay

To detect cell death, the ApopTag Red In Situ Apoptosis Detection Kit (Chemicon) was used in 12-µm-thick cryosections, according to manufacturer's instructions. For full details, see supplementary Materials and Methods.

Immunohistochemistry and PCNA staining

For full details on tissue preparation for immunohistochemistry and antibodies used, see supplementary Materials and Methods.

Fluorescent *in situ* hybridization and immunohistochemistry

For fluorescent *in situ* hybridization combined with immunohistochemistry, 50-µm-thick floating vibratome sections were treated for 12 min with 5 µg/ml proteinase K (Invitrogen) followed by re-fixation for 15 min in 4% PFA-PBS. *In situ* hybridization with digoxigenin-labelled probes was performed as described in detail elsewhere (Wehner et al., 2017). Colour reaction was performed using SIGMAFAST Fast Red (Sigma-Aldrich) substrate. Following termination of the staining reaction by washing sections in PBS containing 0.1% Tween, sections were co-stained using anti-GFP antibody and DAPI to visualize nuclei, mounted in 75% glycerol-PBS and imaged using a Zeiss LSM 780 confocal microscope. Information on *in situ* hybridization probes, including primer sequences used for molecular cloning, and antibodies is provided in the supplementary Materials and Methods and Table S1.

EdU labelling

The 5-ethynyl-2′-deoxyuridine (EdU) nucleoside analogue of thymidine (C10340, Invitrogen) was injected intraperitoneally in adult zebrafish at a concentration of 1.25 mg/ml in PBS and detected at 14 dpl with the Click-iT EdU Alexa Fluor Imaging Kit (Thermo Scientific) according to manufacturer's instructions. For full details, see the supplementary Materials and Methods.

Tissue clearing

Tissue was cleared according to the CUBIC-based clearance technique (Susaki et al., 2014). For full details, see the supplementary Materials and Methods.

Image acquisition and processing

Images were acquired using either an upright Axio Imager.Z2 apotome microscope with a Plan-APOCHROMAT 20×/0.8 NA objective, an upright Leica TCS-SP5 I confocal microscope or an upright Zeiss LSM 780 microscope with an HC PL APO CS 20×/0.7 NA and HCX PL APO 63×/1.2 NA objectives. Images were acquired as *z*-stacks with Zen or Leica software. Cleared tissue images were acquired in tile mode using an upright Zeiss LSM 780 microscope with an LCI Plan Apochromat 25×/0.8 NA water immersion objective. To minimize channel crosstalk, images were acquired sequentially. Images were processed and assembled using Fiji, Imaris, Adobe Photoshop CS6 and Illustrator CS6.

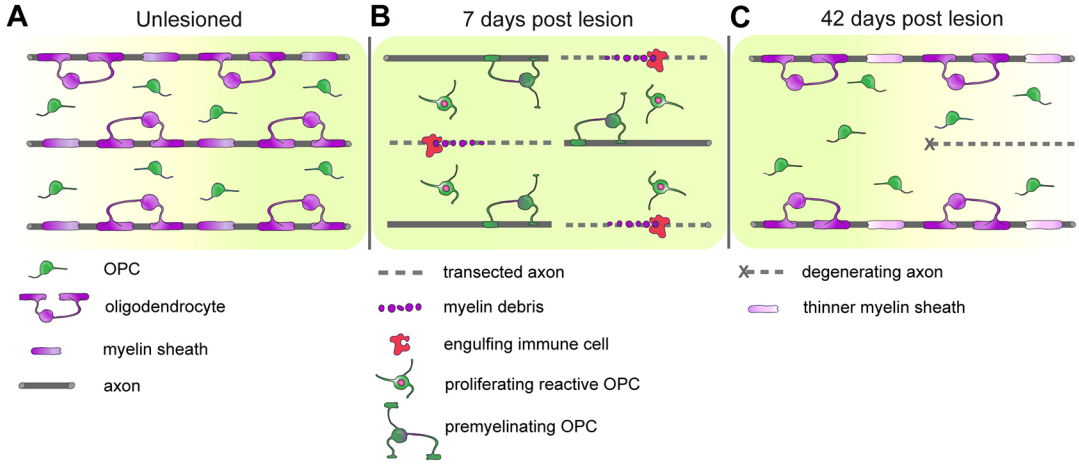

Fig. 9. Contribution of reactive OPCs to zebrafish spinal cord regeneration. (A) In the unlesioned spinal cord, oligodendrocytes ensheath axons and OPCs have thin bipolar processes. Non-myelinated axons and other cell types are omitted for figure clarity. (B) Oligodendrocytes are lost acutely upon lesion, but cellular debris is removed by activated immune cells. OPCs become reactive, proliferate and systemically upregulate genes related to differentiation. A proportion of reactive OPCs becomes pre-myelinating, directly supporting spared axons. (C) Both oligodendrocyte progenitor and oligodendrocyte cell numbers are re-established. At 42 dpl, (re-)myelination is not fully completed, with myelin sheaths that are as yet thinner, compared to pre-injury levels. Some axons are degenerating, while others are still non-myelinated. Nevertheless, partial anatomical and molecular recovery is already sufficient to support the previously reported robust functional recovery at this point in time after lesion (Becker et al., 1997).

Development (2020) 147, dev193946. doi:10.1242/dev.193946

Data quantification and statistical analysis

All cell counts were analysed within 700 µm of the transection site (350 µm rostral and 350 µm caudal) unless otherwise stated. Cells in vibratome sections were manually counted stereologically with the Cell Counter Plugin of Fiji to 50 µm section thickness. Automated cell counting in whole-mount cleared tissue (Fig. 5F-I) was performed in Imaris using the spot detection tool, after 3D-reconstruction. For the TUNEL assay, 12-µm-thick cryosections were taken within 100 µm from the transection site and lesion epicentre (see Fig. S2). Cell profiles were manually counted with the Cell Counter Plugin of Fiji. Every third section was analysed to exclude overrepresentation of the same cell in consecutive counts. Microsoft Excel was used to process the measured data. Graphs are shown as scatter plots with bars depicting the mean and error bars depict s.e.m. (Figs 1, 2C,D, 3, 4, 5, 6 and 8) or box-and-whisker plots (boxes depict the quartiles, whiskers depict 1.5× inter-quartile-range, outliers are plotted as dots) (Fig. 2H,I). Mean refers to the average of at least four counted slices/sections within the lesion or transection site per lesioned fish or at least four counted slices/sections taken from a similar level along the RC axis, in sham control fish. To analyse significance, P values were determined with GraphPad Prism. Details on the statistical test used in each study are given in the figure legends: ****P<0.0001, ***P≤0.001, **P≤0.01 and *P≤0.05; P>0.05 was not considered significant.

Spinal cord dissection and dissociation

Adult fish were terminally anaesthetized in 0.1% w/vol Tricaine (Sigma Aldrich) in E3 solution with 10^{-5}% v/v Methylene Blue. The skin and musculature were removed dorsally until the spinal cord was exposed and carefully removed with fine forceps. Extracted tissue was placed on a microscope scale slide (474026, Carl Zeiss); starting from the lesion site, a ∼0.5 mm piece was cut from the rostral part with a scalpel. For sham control group, a ∼0.5 mm tissue was dissected at the same area of the spinal cord along the rostral to caudal axis of the fish. Nine spinal cords (∼0.5 mm pieces) were used per group and placed in 1 ml of sterile Hanks' buffered salt solution (HBSS) (Gibco). Before tissue dissociation, spinal cords were kept on ice continuously to avoid cell degradation. Tissue dissociation, live cell staining and FACS of cells was carried out with modifications using an unpublished protocol developed by the Brand lab (D. Freudenreich, A. Weber and M. Brand., unpublished and Lange et al., 2020). Briefly, excised tissue was dissociated with the Neural Tissue Dissociation Kit (130-092-628, Miltenyi Bioscience) by incubating for 15 min at 37°C in dissociation buffer. Tissue digestion was stopped by the addition of 30 µl of Papain inhibitor, triturated with 10 strokes of a wide-tipped fire-polished Pasteur pipette and incubated at 37°C for 10 min. After two more trituration steps with 10 strokes of a middle and small-tipped fire-polished Pasteur pipette, respectively, and incubation for 10 min at 37°C, cell suspension was applied to a 20 µm cell strainer (BD Biosciences), mounted in a 15 ml falcon tube. After washing with 10 ml of sterile HBSS, the cell suspension was pelleted by centrifugation at 300 ***g*** for 10 min at room temperature. The supernatant was discarded and the pellet was re-suspended in 500 µl fresh sterile HBSS. To stain for viable cells, 1 µl of 2 mM Calcein Blue-AM (C1429, Invitrogen) was added to the cell suspension. The cell suspension was protected from light and incubated for 10 min at room temperature until fluorescence-activated cell sorting was carried out.

Fluorescence activated cell sorting of adult zebrafish OPCs

Adult zebrafish OPCs were sorted using a BD FACSAria sorter. For the detection of GFP a 488 nm excitation laser and a 530/30 bandpass filter were used. Calcein Blue-AM was detected after 405 nm excitation using a 450/40 nm bandpass emission filter. Cellular events were defined by forward- and side-scatter profile, and by the GFP signal of the transgenic line. From this selection, all events that showed incorporation of the Calcein Blue-AM were finally gated and sorted.

Deep sequencing and data analysis

RNAseq was based on Smart-seq2 sensitive full-length transcriptome profiling and modified from Picelli et al. (2013). Briefly, either one or 30 GFP^+ cells from Tg(*olig2*:$eGFP^+$) fish were FAC sorted into single wells of a 96-well plate containing 2 µl of nuclease-free water with 0.2% (v/v) Triton-X 100 and 4 U murine RNase Inhibitor (NEB), spun down and frozen at −80°C. After thawing the samples, 2 µl of a primer mix was added. RNA was then denatured for 3 min at 72°C and the reverse transcription was performed at 42°C for 90 min after filling up to 10 µl with reverse transcription buffer mix. The reverse transcriptase was inactivated at 70°C for 15 min and the cDNA was amplified using Kapa HiFi HotStart Readymix (Peqlab) at a final 1× concentration and 0.1 µM UP-primer (UP-primer:AAGCAGTGGTATCAACGCAGAGT). The amplified cDNA was then purified using 1× volume of hydrophobic Sera-Mag SpeedBeads (GE Healthcare) and DNA was eluted in 12 µl nuclease-free water. The concentration of the samples was measured with a Tecan plate reader Infinite 200 pro in 384 well black flat bottom low volume plates (Corning) using AccuBlue Broad range chemistry (Biotium). For library preparation, 700 pg cDNA in 2 µl were mixed with 0.5 µl Tagment DNA Enzyme, 2.5 µl Tagment DNA Buffer (Nextera, Illumina) and tagmented at 55°C for 5 min. Subsequently, Illumina indices were added during PCR with 1× concentrated KAPA Hifi HotStart Ready Mix and 0.7 µM dual indexing primers. After PCR, libraries were quantified with AccuBlue Broad range chemistry, equimolarly pooled and purified twice with 1× volume Sera-Mag SpeedBeads. This was followed by Illumina sequencing on a Nextseq500, aiming at an average sequencing depth of 0.5 million reads per cell. Gene ontology was performed with DAVID 6.8 Functional Annotation Tool (NIAID/NIH).

Acknowledgements

We thank Claudia Froeb for maintaining zebrafish colonies and outstanding technical support, Dr René Bernitz (CRTD, Dresden) for the *tnc in situ* hybridization probe and Catherina G. Becker for critical reading of the manuscript. This work was supported by the Flow Cytometry Facility, the Light Microscopy Facility, the Electron Microscopy Facility, the Deep Sequencing Facility and the Zebrafish Facility at CRTD of Technische Universität Dresden. The Sächsisches Ministerium für Wissenschaft und Kunst supported this project through grants to the light microscopy and electron microscopy facilities at CMCB, TU Dresden (European Fund for Regional Development - EFRE).

Competing interests

The authors declare no competing or financial interests.

Author contributions

Conceptualization: V.T., M.M.R., M.B.; Formal analysis: V.T., V.K., F.R., S.R., A.P.; Investigation: V.T., V.K., D.W., F.R., C.L., C.H., T.K., S.R., A.P., M.L.; Resources: A.D., M.M.R., M.B.; Writing - original draft: V.T., M.B.; Writing - review & editing: V.T., V.K., D.W., M.B.; Visualization: V.T.

Funding

We gratefully acknowledge support from the Deutsche Forschungsgemeinschaft through a centre grant to the Center for Regenerative Therapies Dresden as DFG Forschungszentrum and Cluster of Excellence (FZ 111 and DFG EXC 168), and the support of a Deutsche Forschungsgemeinschaft grant (BR 1746/11-1) and a Center for Regenerative Therapies Dresden seed grant (DFG FZT 111/3) to M.B. D.W. received a Rückkehrstipendium from Deutsche Forschungsgemeinschaft (WE5736/2-1). The European Union and Bundesministerium für Bildung und Forschung supported this project through grants to M.M.R. and M.B. (ERA-NET NEURON NeuroNiche project 01EW1708A) and a European Research Council advanced grant (Zf-BrainReg) to M.B.

Data availability

The RNA-seq data reported in this article have been deposited in Gene Expression Omnibus under accession number GSE161687.

Supplementary information

Supplementary information available online at
https://dev.biologists.org/lookup/doi/10.1242/dev.193946.supplemental

References

Aggarwal, S., Yurlovas5, L., Snaidero, N., Reetz, C., Frey, S., Zimmermann, J., Pähler, G., Janshoff, A., Friedrichs, J., Müller, D. J. et al. (2011). A size barrier limits protein diffusion at the cell surface to generate lipid-rich myelin-membrane sheets. *Dev. Cell* **21**, 445-456. doi:10.1016/j.devcel.2011.08.001

Almeida, R. G., Czopka, T., Ffrench-Constant, C. and Lyons, D. A. (2011). Individual axons regulate the myelinating potential of single oligodendrocytes in vivo. *Development* **138**, 4443-4450. doi:10.1242/dev.071001

Auer, F., Vagionitis, S. and Czopka, T. (2018). Evidence for myelin sheath remodeling in the CNS revealed by in vivo imaging. *Curr. Biol.* **28**, 549-559.e543. doi:10.1016/j.cub.2018.01.017

Bacmeister, C. M., Barr, H. J., McClain, C. R., Thornton, M. A., Nettles, D., Welle, C. G. and Hughes, E. G. (2020). Motor learning promotes remyelination via new and surviving oligodendrocytes. *Nat. Neurosci.* **23**, 819-831. doi:10.1101/2020.01.28.923656

Becker, T. and Becker, C. G. (2001). Regenerating descending axons preferentially reroute to the gray matter in the presence of a general macrophage/microglial reaction caudal to a spinal transection in adult zebrafish. *J. Comp. Neurol.* **433**, 131-147. doi:10.1002/cne.1131

Becker, T., Wullimann, M. F., Becker, C. G., Bernhardt, R. R. and Schachner, M. (1997). Axonal regrowth after spinal cord transection in adult zebrafish. *J. Comp. Neurol.* **377**, 577-595. doi:10.1002/(SICI)1096-9861(19970127)377:4<577::AID-CNE8>3.0.CO;2-#

Becker, C. G., Lieberoth, B. C., Morellini, F., Feldner, J., Becker, T. and Schachner, M. (2004). L1.1 is involved in spinal cord regeneration in adult zebrafish. *J. Neurosci.* **24**, 7837-7842. doi:10.1523/JNEUROSCI.2420-04.2004

Becker, T., Lieberoth, B. C., Becker, C. G. and Schachner, M. (2005). Differences in the regenerative response of neuronal cell populations and indications for plasticity in intraspinal neurons after spinal cord transection in adult zebrafish. *Mol. Cell. Neurosci.* **30**, 265-278. doi:10.1016/j.mcn.2005.07.008

Brand, M., Granato, M. and Nüsslein-Volhard, C. (2002). Keeping and raising zebrafish. In *Zebrafish: A Practical Approach* (ed. C. Nüsslein-Volhard and R. Dahm), pp. 7-37. Oxford: Oxford University Press.

Bunge, M. B., Bunge, R. P. and Ris, H. (1961). Ultrastructural study of remyelination in an experimental lesion in adult cat spinal cord. *J. Biophys. Biochem. Cytol.* **10**, 67-94. doi:10.1083/jcb.10.1.67

Cao, Q., Xu, X. M., Devries, W. H., Enzmann, G. U., Ping, P., Tsoulfas, P., Wood, P. M., Bunge, M. B. and Whittemore, S. R. (2005). Functional recovery in traumatic spinal cord injury after transplantation of multineurotrophin-expressing glial-restricted precursor cells. *J. Neurosci.* **25**, 6947-6957. doi:10.1523/JNEUROSCI.1065-05.2005

Cigliola, V., Becker, C. J. and Poss, K. D. (2020). Building bridges, not walls: spinal cord regeneration in zebrafish. *Dis. Model. Mech.* **13**, dmm044131. doi:10.1242/dmm.044131

Crowe, M. J., Bresnahan, J. C., Shuman, S. L., Masters, J. N. and Beattie, M. S. (1997). Apoptosis and delayed degeneration after spinal cord injury in rats and monkeys. *Nat. Med.* **3**, 73-76. doi:10.1038/nm0197-73

Czopka, T., Ffrench-Constant, C. and Lyons, D. A. (2013). Individual oligodendrocytes have only a few hours in which to generate new myelin sheaths in vivo. *Dev. Cell* **25**, 599-609. doi:10.1016/j.devcel.2013.05.013

Duncan, I. D., Marik, R. L., Broman, A. T. and Heidari, M. (2017). Thin myelin sheaths as the hallmark of remyelination persist over time and preserve axon function. *Proc. Natl Acad. Sci. USA* **114**, E9685-E9691. doi:10.1073/pnas.1714183114

Duncan, G. J., Manesh, S. B., Hilton, B. J., Assinck, P., Liu, J., Moulson, A., Plemel, J. R. and Tetzlaff, W. (2018a). Locomotor recovery following contusive spinal cord injury does not require oligodendrocyte remyelination. *Nat. Commun.* **9**, 3066. doi:10.1038/s41467-018-05473-1

Duncan, I. D., Radcliff, A. B., Heidari, M., Kidd, G., August, B. K. and Wierenga, L. A. (2018b). The adult oligodendrocyte can participate in remyelination. *Proc. Natl Acad. Sci. USA* **115**, E11807-E11816. doi:10.1073/pnas.1808064115

Filous, A. R., Tran, A., Howell, C. J., Busch, S. A., Evans, T. A., Stallcup, W. B., Kang, S. H., Bergles, D. E., Lee, S.-I., Levine, J. M. et al. (2014). Entrapment via synaptic-like connections between NG2 proteoglycan+ cells and dystrophic axons in the lesion plays a role in regeneration failure after spinal cord injury. *J. Neurosci.* **34**, 16369-16384. doi:10.1523/JNEUROSCI.1309-14.2014

Foerster, S., Neumann, B., McClain, C., Di Canio, L., Chen, C. Z., Reich, D. S., Simons, B. D. and Franklin, R. J. (2020). Proliferation is a requirement for differentiation of oligodendrocyte progenitor cells during CNS remyelination. *bioRxiv*, 2020.2005.2021.108373.

Fok-Seang, J., Smith-Thomas, L. C., Meiners, S., Muir, E., Du, J. S., Housden, E., Johnson, A. R., Faissner, A., Geller, H. M., Keynes, R. J. et al. (1995). An analysis of astrocytic cell lines with different abilities to promote axon growth. *Brain Res.* **689**, 207-223. doi:10.1016/0006-8993(95)00575-B

Franklin, R. J. M., Gilson, J. M. and Blakemore, W. F. (1997). Local recruitment of remyelinating cells in the repair of demyelination in the central nervous system. *J. Neurosci. Res.* **50**, 337-344. doi:10.1002/(SICI)1097-4547(19971015)50:2<337::AID-JNR21>3.0.CO;2-3

Fünfschilling, U., Supplie, L. M., Mahad, D., Boretius, S., Saab, A. S., Edgar, J., Brinkmann, B. G., Kassmann, C. M., Tzvetanova, I. D., Möbius, W. et al. (2012). Glycolytic oligodendrocytes maintain myelin and long-term axonal integrity. *Nature* **485**, 517-521. doi:10.1038/nature11007

Goebbels, S., Wieser, G. L., Pieper, A., Spitzer, S., Weege, B., Yan, K., Edgar, J. M., Yagensky, O., Wichert, S. P., Agarwal, A. et al. (2017). A neuronal PI(3,4,5)P(3)-dependent program of oligodendrocyte precursor recruitment and myelination. *Nat. Neurosci.* **20**, 10-15. doi:10.1038/nn.4425

Gonzalez, G. A., Hofer, M. P., Syed, Y. A., Amaral, A. I., Rundle, J., Rahman, S., Zhao, C. and Kotter, M. R. N. (2016). Tamoxifen accelerates the repair of demyelinated lesions in the central nervous system. *Sci. Rep.* **6**, 31599. doi:10.1038/srep31599

Guest, J. D., Hiester, E. D. and Bunge, R. P. (2005). Demyelination and Schwann cell responses adjacent to injury epicenter cavities following chronic human spinal cord injury. *Exp. Neurol.* **192**, 384-393. doi:10.1016/j.expneurol.2004.11.033

Habgood, M. D., Bye, N., Dziegielewska, K. M., Ek, C. J., Lane, M. A., Potter, A., Morganti-Kossmann, C. and Saunders, N. R. (2007). Changes in blood-brain barrier permeability to large and small molecules following traumatic brain injury in mice. *Eur. J. Neurosci.* **25**, 231-238. doi:10.1111/j.1460-9568.2006.05275.x

Huang, J. K., Jarjour, A. A., Nait Oumesmar, B., Kerninon, C., Williams, A., Krezel, W., Kagechika, H., Bauer, J., Zhao, C., Baron-Van Evercooren, A. et al. (2011). Retinoid X receptor gamma signaling accelerates CNS remyelination. *Nat. Neurosci.* **14**, 45-53. doi:10.1038/nn.2702

Hughes, E. G., Kang, S. H., Fukaya, M. and Bergles, D. E. (2013). Oligodendrocyte progenitors balance growth with self-repulsion to achieve homeostasis in the adult brain. *Nat. Neurosci.* **16**, 668-676. doi:10.1038/nn.3390

Jung, S.-H., Kim, S., Chung, A.-Y., Kim, H.-T., So, J.-H., Ryu, J., Park, H.-C. and Kim, C.-H. (2010). Visualization of myelination in GFP-transgenic zebrafish. *Dev. Dyn.* **239**, 592-597. doi:10.1002/dvdy.22166

Káradóttir, R., Hamilton, N. B., Bakiri, Y. and Attwell, D. (2008). Spiking and nonspiking classes of oligodendrocyte precursor glia in CNS white matter. *Nat. Neurosci.* **11**, 450-456. doi:10.1038/nn2060

Karttunen, M. J., Czopka, T., Goedhart, M., Early, J. J. and Lyons, D. A. (2017). Regeneration of myelin sheaths of normal length and thickness in the zebrafish CNS correlates with growth of axons in caliber. *PLoS ONE* **12**, e0178058. doi:10.1371/journal.pone.0178058

Kaslin, J., Ganz, J. and Brand, M. (2008). Proliferation, neurogenesis and regeneration in the non-mammalian vertebrate brain. *Philos. Trans. R. Soc. Lond. B Biol. Sci.* **363**, 101-122. doi:10.1098/rstb.2006.2015

Keirstead, H. S. and Blakemore, W. F. (1997). Identification of post-mitotic oligodendrocytes incapable of remyelination within the demyelinated adult spinal cord. *J. Neuropathol. Exp. Neurol.* **56**, 1191-1201. doi:10.1097/00005072-199711000-00003

Keirstead, H. S., Levine, J. M. and Blakemore, W. F. (1998). Response of the oligodendrocyte progenitor cell population (defined by NG2 labelling) to demyelination of the adult spinal cord. *Glia* **22**, 161-170. doi:10.1002/(SICI)1098-1136(199802)22:2<161::AID-GLIA7>3.0.CO;2-A

Keirstead, H. S., Nistor, G., Bernal, G., Totoiu, M., Cloutier, F., Sharp, K. and Steward, O. (2005). Human embryonic stem cell-derived oligodendrocyte progenitor cell transplants remyelinate and restore locomotion after spinal cord injury. *J. Neurosci.* **25**, 4694-4705. doi:10.1523/JNEUROSCI.0311-05.2005

Koudelka, S., Voas, M. G., Almeida, R. G., Baraban, M., Soetaert, J., Meyer, M. P., Talbot, W. S. and Lyons, D. A. (2016). Individual neuronal subtypes exhibit diversity in CNS myelination mediated by synaptic vesicle release. *Curr. Biol.* **26**, 1447-1455. doi:10.1016/j.cub.2016.03.070

Kroehne, V., Freudenreich, D., Hans, S., Kaslin, J. and Brand, M. (2011). Regeneration of the adult zebrafish brain from neurogenic radial glia-type progenitors. *Development* **138**, 4831-4841. doi:10.1242/dev.072587

Kroehne, V., Tsata, V., Marrone, L., Froeb, C., Reinhardt, S., Gompf, A., Dahl, A., Sterneckert, J. and Reimer, M. M. (2017). Primary spinal OPC culture system from adult zebrafish to study oligodendrocyte differentiation in vitro. *Front. Cell Neurosci.* **11**, 284. doi:10.3389/fncel.2017.00284

Kuscha, V., Barreiro-Iglesias, A., Becker, C. G. and Becker, T. (2012). Plasticity of tyrosine hydroxylase and serotonergic systems in the regenerating spinal cord of adult zebrafish. *J. Comp. Neurol.* **520**, 933-951. doi:10.1002/cne.22739

Kyritsis, N., Kizil, C., Zocher, S., Kroehne, V., Kaslin, J., Freudenreich, D., Iltzsche, A. and Brand, M. (2012). Acute inflammation initiates the regenerative response in the adult zebrafish brain. *Science* **338**, 1353-1356. doi:10.1126/science.1228773

Lange, C., Rost, F., Machate, A., Reinhardt, S., Lesche, M., Weber, A., Kuscha, V., Dahl, A., Rulands, S. and Brand, M. (2020). Single cell sequencing of radial glia progeny reveals the diversity of newborn neurons in the adult zebrafish brain. *Development* **147**, dev185595. doi:10.1242/dev.185595

Llorens-Bobadilla, E., Chell, J. M., Le Merre, P., Wu, Y., Zamboni, M., Bergenstråhle, J., Stenudd, M., Sopova, E., Lundeberg, J., Shupliakov, O. et al. (2020). A latent lineage potential in resident neural stem cells enables spinal cord repair. *Science* **370**, eabb8795. doi:10.1126/science.abb8795

Ludwin, S. K. and Maitland, M. (1984). Long-term remyelination fails to reconstitute normal thickness of central myelin sheaths. **64**, 193-198. doi:10.1016/0022-510x(84)90037-6

Marisca, R., Hoche, T., Agirre, E., Hoodless, L. J., Barkey, W., Auer, F., Castelo-Branco, G. and Czopka, T. (2020). Functionally distinct subgroups of oligodendrocyte precursor cells integrate neural activity and execute myelin formation. *Nat. Neurosci.* **23**, 363-374. doi:10.1038/s41593-019-0581-2

Mason, J. L., Toews, A., Hostettler, J. D., Morell, P., Suzuki, K., Goldman, J. E. and Matsushima, G. K. (2004). Oligodendrocytes and progenitors become progressively depleted within chronically demyelinated lesions. *Am. J. Pathol.* **164**, 1673-1682. doi:10.1016/S0002-9440(10)63726-1

Mensch, S., Baraban, M., Almeida, R., Czopka, T., Ausborn, J., El Manira, A. and Lyons, D. A. (2015). Synaptic vesicle release regulates myelin sheath number of individual oligodendrocytes in vivo. *Nat. Neurosci.* **18**, 628. doi:10.1038/nn.3991

Mokalled, M. H., Patra, C., Dickson, A. L., Endo, T., Stainier, D. Y. R. and Poss, K. D. (2016). Injury-induced ctgfa directs glial bridging and spinal cord regeneration in zebrafish. *Science* **354**, 630-634. doi:10.1126/science.aaf2679

Moyon, S., Dubessy, A. L., Aigrot, M. S., Trotter, M., Huang, J. K., Dauphinot, L., Potier, M. C., Kerninon, C., Melik Parsadaniantz, S., Franklin, R. J. M. et al. (2015). Demyelination causes adult CNS progenitors to revert to an immature state and express immune cues that support their migration. *J. Neurosci.* **35**, 4-20. doi:10.1523/JNEUROSCI.0849-14.2015

Münzel, E. J., Becker, C. G., Becker, T. and Williams, A. (2014). Zebrafish regenerate full thickness optic nerve myelin after demyelination, but this fails with increasing age. *Acta Neuropathol. Commun.* **2**, 77. doi:10.1186/s40478-014-0077-y

Neely, S. A., Williamson, J. M., Klingseisen, A., Zoupi, L., Early, J. J., Williams, A. and Lyons, D. A. (2020). New oligodendrocytes exhibit more abundant and accurate myelin regeneration than those that survive demyelination. *bioRxiv*, 2020.2005.2022.110551.

Neumann, H., Kotter, M. R. and Franklin, R. J. M. (2009). Debris clearance by microglia: an essential link between degeneration and regeneration. *Brain* **132**, 288-295. doi:10.1093/brain/awn109

Neumann, B., Baror, R., Zhao, C., Segel, M., Dietmann, S., Rawji, K. S., Foerster, S., McClain, C. R., Chalut, K., van Wijngaarden, P. et al. (2019). Metformin restores CNS remyelination capacity by rejuvenating aged stem cells. *Cell Stem Cell* **25**, 473-485.e478. doi:10.1016/j.stem.2019.08.015

Ohnmacht, J., Yang, Y., Maurer, G. W., Barreiro-Iglesias, A., Tsarouchas, T. M., Wehner, D., Sieger, D., Becker, C. G. and Becker, T. (2016). Spinal motor neurons are regenerated after mechanical lesion and genetic ablation in larval zebrafish. *Development* **143**, 1464-1474. doi:10.1242/dev.129155

Ono, K., Kagawa, T., Tsumori, T., Yokota, S. and Yasui, Y. (2001). Morphological changes and cellular dynamics of oligodendrocyte lineage cells in the developing vertebrate central nervous system. *Dev. Neurosci.* **23**, 346-355. doi:10.1159/000048718

Papastefanaki, F. and Matsas, R. (2015). From demyelination to remyelination: the road toward therapies for spinal cord injury. *Glia* **63**, 1101-1125. doi:10.1002/glia.22809

Payne, S. C., Bartlett, C. A., Savigni, D. L., Harvey, A. R., Dunlop, S. A. and Fitzgerald, M. (2013). Early proliferation does not prevent the loss of oligodendrocyte progenitor cells during the chronic phase of secondary degeneration in a CNS white matter tract. *PLoS ONE* **8**, e65710. doi:10.1371/journal.pone.0065710

Pedraza, C. E., Taylor, C., Pereira, A., Seng, M., Tham, C.-S., Izrael, M. and Webb, M. (2014). Induction of oligodendrocyte differentiation and in vitro myelination by inhibition of rho-associated kinase. *ASN neuro* **6**, 1759091414538134. doi:10.1177/1759091414538134

Picelli, S., Björklund, A. K., Faridani, O. R., Sagasser, S., Winberg, G. and Sandberg, R. (2013). Smart-seq2 for sensitive full-length transcriptome profiling in single cells. *Nat. Methods* **10**, 1096-1098. doi:10.1038/nmeth.2639

Plemel, J. R., Manesh, S. B., Sparling, J. S. and Tetzlaff, W. (2013). Myelin inhibits oligodendroglial maturation and regulates oligodendrocytic transcription factor expression. *Glia* **61**, 1471-1487. doi:10.1002/glia.22535

Powers, B. E., Sellers, D. L., Lovelett, E. A., Cheung, W., Aalami, S. P., Zapertov, N., Maris, D. O. and Horner, P. J. (2013). Remyelination reporter reveals prolonged refinement of spontaneously regenerated myelin. *Proc. Natl. Acad. Sci. USA* **110**, 4075-4080. doi:10.1073/pnas.1210293110

Raine, C. S. and Cross, A. H. (1989). Axonal dystrophy as a consequence of long-term demyelination. *Lab. Investig.* **60**, 714-725.

Reimer, M. M., Sorensen, I., Kuscha, V., Frank, R. E., Liu, C., Becker, C. G. and Becker, T. (2008). Motor neuron regeneration in adult zebrafish. *J. Neurosci.* **28**, 8510-8516. doi:10.1523/JNEUROSCI.1189-08.2008

Romanelli, E., Merkler, D., Mezydlo, A., Weil, M.-T., Weber, M. S., Nikić, I., Potz, S., Meinl, E., Matznick, F. E. H., Kreutzfeldt, M. et al. (2016). Myelinosome formation represents an early stage of oligodendrocyte damage in multiple sclerosis and its animal model. *Nat. Commun.* **7**, 13275. doi:10.1038/ncomms13275

Shin, J., Park, H.-C., Topczewska, J. M., Mawdsley, D. J. and Appel, B. (2003). Neural cell fate analysis in zebrafish using olig2 BAC transgenics. *Methods Cell Sci.* **25**, 7-14. doi:10.1023/B:MICS.0000006847.09037.3a

Sim, F. J., Zhao, C., Penderis, J. and Franklin, R. J. M. (2002). The age-related decrease in CNS remyelination efficiency is attributable to an impairment of both oligodendrocyte progenitor recruitment and differentiation. *J. Neurosci.* **22**, 2451-2459. doi:10.1523/JNEUROSCI.22-07-02451.2002

Smith, K. J., Blakemore, W. F. and McDonald, W. I. (1979). Central remyelination restores secure conduction. *Nature* **280**, 395-396. doi:10.1038/280395a0

Susaki, E. A., Tainaka, K., Perrin, D., Kishino, F., Tawara, T., Watanabe, T. M., Yokoyama, C., Onoe, H., Eguchi, M., Yamaguchi, S. et al. (2014). Whole-brain imaging with single-cell resolution using chemical cocktails and computational analysis. *Cell* **157**, 726-739. doi:10.1016/j.cell.2014.03.042

Totoiu, M. O. and Keirstead, H. S. (2005). Spinal cord injury is accompanied by chronic progressive demyelination. *J. Comp. Neurol.* **486**, 373-383. doi:10.1002/cne.20517

Tsarouchas, T. M., Wehner, D., Cavone, L., Munir, T., Keatinge, M., Lambertus, M., Underhill, A., Barrett, T., Kassapis, E., Ogryzko, N. et al. (2018). Dynamic control of proinflammatory cytokines Il-1β and Tnf-α by macrophages in zebrafish spinal cord regeneration. *Nat. Commun.* **9**, 4670. doi:10.1038/s41467-018-07036-w

Tsata, V., Kroehne, V., Reinhardt, S., El-Armouche, A., Brand, M., Wagner, M. and Reimer, M. M. (2019). Electrophysiological properties of adult zebrafish oligodendrocyte progenitor cells. *Front. Cell. Neurosci.* **13**, 102. doi:10.3389/fncel.2019.00102

Wehner, D., Tsarouchas, T. M., Michael, A., Haase, C., Weidinger, G., Reimer, M. M., Becker, T. and Becker, C. G. (2017). Wnt signaling controls pro-regenerative Collagen XII in functional spinal cord regeneration in zebrafish. *Nat. Commun.* **8**, 126. doi:10.1038/s41467-017-00143-0

Yeung, M. S. Y., Djelloul, M., Steiner, E., Bernard, S., Salehpour, M., Possnert, G., Brundin, L. and Frisén, J. (2019). Dynamics of oligodendrocyte generation in multiple sclerosis. *Nature* **566**, 538-542. doi:10.1038/s41586-018-0842-3

SUPPLEMENTARY MATERIALS AND METHODS

Electron microscopy

Tg(*mbp*:eGFP) adult fish (sham, 7 dpl and 42 dpl) were terminally anesthetized in 0.1% w/vol Tricaine (Sigma-Aldrich), fixed by injection of modified Karnovsky's fixative (2% glutaraldehyde, 2% paraformaldehyde in 150 mM cacodylate buffer) into the vascular system and kept in fixative for at least 2 hours at room temperature. Fixed spinal cord tissue was then dissected out and kept in fixative at 4°C overnight. Samples were washed twice in cacodylate buffer and twice in water. Samples were postfixed in 2% aqueous OsO_4 solution containing 1.5% potassium ferrocyanide and 2 mM $CaCl_2$ for 30 min on ice, followed by washes in water, incubation in 1% thiocarbohydrazide in water (20 min at room temperature), washed again in water and a second osmium contrasting step in 2% OsO_4/water (30 min, on ice). After several washes in water, the samples were *en bloc* contrasted with 1% uranyl acetate/water for 2 hours on ice, washed again in water, dehydrated in a graded series of ethanol/water up to 100% ethanol, and infiltrated in epon 812 (epon/ethanol mixtures: 1:3, 1:1, 3:1 for 1.5 hours each, pure epon overnight, pure epon 5 hours). Samples were embedded in flat embedding molds and cured at 65°C overnight. To identify the section level of interest (within 50 µm rostral to the lesion site) semithin sections were prepared with a Leica UC6 ultramicrotome using glass knifes and stained with 1% toluidine blue/0.5% borax. Ultrathin sections at the level of interest were prepared using a diamond knife, collected on formvar-coated slot grids and stained with lead citrate (Venable and Coggeshall, 1965). Contrasted ultrathin sections were analyzed on a FEI Morgagni D268 (FEI, Eindhoven, The Netherlands) or a Jeol JEM1400 Plus at 80 kV acceleration voltage.
For the 1 ypl timepoint, the lesion site was not apparent externally and also not visible on the dissected spinal cord itself. To identify the lesion site before targeted ultramicrotomy and TEM analysis, we performed X-ray microtomography (XµCT) on the epon embedded samples, an approach recently developed for several soft tissue samples (Metscher, 2009; Handschuh, 2013; Minarik M, 2017). For the scan, most of the epon around the sample was cut away and the small blocks were glued to the head of a needle. XµCT was performed with the Zeiss XRadia 520 Versa (Carl Zeiss AG, Oberkochen, Germany) using the following parameters: Scan medium: air; Filter: LE1; Optical magnification: 4x; Distance source-sample: 10 mm; Distance source-detector: 25 mm; Exposure time 20 s/image; Number of images: 2950; Binning: 1; pixel size:

0,996 µm. The X-ray scan was reconstructed as a TIFF-stack and the position of the lesion site was determined based on the size of the ventricle along the anterior-posterior axis of the spinal cord. The spinal cords were then remounted on empty epon dummy blocks for ultrathin sectioning. Correct orientation and position of the tissue in the block was controlled several times on toluidine blue/borax stained semithin sections and compared to the corresponding TIFF-stack images of the XµCT scan. Once the lesion site was reached, ultrathin sections were prepared and imaged at the TEM.

Tissue preparation for *in situ* hybridization, immunohistochemistry and CUBIC-based clearing

Adult fish were terminally anesthetized in 0.1% w/vol Tricaine (Sigma-Aldrich) in PBS, fixed by injection of 4% paraformaldehyde solution (PFA) (methanol-free) (Agar Scientific) in PBS into the vascular system and post-fixed in 4% PFA overnight, at 4°C. Fixed tissue was extracted, washed in PBS and either cut in 50 µm-thick transverse vibratome sections (VT 1200S, Leica), 12 µm-thick transverse cryosections (Cryostat HM 560, Microm) or processed whole-mount.

Table S1. Source of *in situ* hybridization probe templates and primers used to generate *in situ* hybridization probe templates.

Gene	ENSEMBL ID	Source	Primer
tnc	ENSDARG00000021948	René Bernitz, CRTD Dresden	-
ctgfa	ENSDARG00000042934	this study	(S) TGTGATTGCTCTGCTGTTCC (AS) GGTGAGGCGATTAGCTTCTG
apoeb	ENSDARG00000040295	this study	(S) ATTACTGACACCATGGCTGAACT (AS) AGTGCTAGTCCAATTGAGTCCAG
sema3c	ENSDARG00000034300	this study	(S) ACGAAAAACATTCATGCCATGGT (AS) GTTGGTAATGGGAGACTGTGTCT

TUNEL cell death assay

Fixed fish were transferred for decalcification and cryo-protection to 20% sucrose/20% EDTA in 0.1 M phosphate buffer pH 7.5, overnight, at 4°C. Fish were further cryo-protected in 7.5% gelatin/20% sucrose in 0.1 M phosphate buffer pH 7.5, at 37°C, frozen in the same solution as a whole and finally sectioned with a rostral to caudal

direction into 12 µm cryosections (Fig. S2). Cryosections were mounted on fat-free superfrost glass slides (StarFrost®, Engelbrecht). For the detection of cell death, the ApopTag Red In Situ Apoptosis Detection Kit (Chemicon), was used according to manufacturer's instructions. A positive (digestion with DNase I (3000-3 U/mL) in 50 mM TrisHCl, pH 7.5, 1 mg/mL BSA) and negative (omitting the TdT enzyme) control slide was included.

Immunohistochemistry

Primary antibodies were mouse monoclonal against PCNA (PC 10, 1:500, Dako); rabbit polyclonal against L-Plastin (custom-made, expression plasmid provided by Michael J. Redd, 1:7500); rabbit polyclonal against Neurofilament 200 (N4142, 1:500, Sigma-Aldrich); rat monoclonal against Claudin K (not commercially available, 1:500, (Munzel et al., 2012)); mouse monoclonal against GFAP (MAB3402, 1:1000, Merck) and chicken polyclonal against GFP (ab13970, 1:3000 and 1:6000, Abcam). For detection, Alexa Fluor® 555 (A21424, 1:750, Invitrogen), Cy™3 (711-165-152, 1:200, Jackson ImmunoResearch Europe Ltd) and Alexa Fluor® 488 (103-545-155, 1:750, Jackson ImmunoResearch Europe Ltd.) conjugated secondary antibodies were used, respectively. Antibodies were incubated in PBS with 0.5% Triton-X. Primary antibodies were incubated overnight at 4°C and secondary antibodies for 2 hours at room temperature.

PCNA staining

To retrieve the antigen for the PCNA staining, vibratome sections were incubated floating in 10 mM Sodium Citrate Buffer pH 6, at 85°C for 20 min. Sections were left to cool down at room temperature, washed with PBS for 10 min and then twice in PBS with 0.5% Triton-X. As the antigen retrieval step quenches endogenous fluorescence when PCNA is used in an endogenously fluorescent transgenic line (i.e Tg(*olig2*:eGFP), an anti-GFP enhancement step was included in the protocol and carried out before (1:3000) and after the antigen retrieval (1:6000).

Tissue clearing

Fixed tissue was washed 3 times for 30 min in PBS with 0.3% Triton-X and then immersed in CUBIC-1 solution overnight, at room temperature. Tissue was thoroughly washed in PBS with 0.3% Triton-X for 3 times for 30 min and immersed in increasing concentrations (vol/vol) of CUBIC-2 solution (25%, 50%, 75% vol/vol in PBS) for 1 hour each and an overnight incubation in 100% CUBIC-1 at room temperature, for final clearing. Tissue was mounted in CUBIC-2 solution in superfrost glass slides (StarFrost®, Engelbrecht) and imaged directly to avoid quenching of endogenous fluorescence. Detection of EdU and nuclear staining with 0.3 µM DAPI (#6335.1, Roth) in PBS took place after incubation in CUBIC-1.

EdU labelling

To monitor cells in the S-phase of the cell cycle after SCI, the 5-ethynyl-2'-deoxyuridine (EdU) nucleoside analog of thymidine (C10340, Invitrogen) was injected intraperitoneally in adult zebrafish at a concentration of 1.25 mg/ml in PBS. Injections started at 5 dpl and took place every 48 hours, for three (Tg(*mbp*:eGFP)) or five (Tg(*olig2*:eGFP)) times. Proliferating cells were detected at 14 dpl with the Click-iT™ EdU Alexa Fluor™ Imaging Kit (Thermo Scientific) according to manufacturer's instructions in either 50 µm-thick vibratome sections or whole-mount tissue after CUBIC-based tissue clearing.

Supplemental Figures

Figure S1

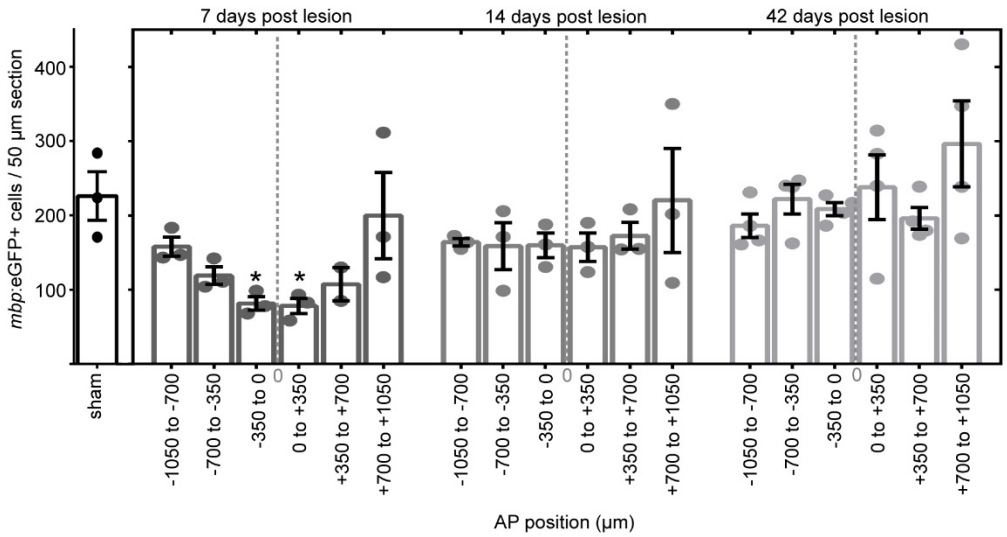

Figure S1. Spinal cord transection results in a spatially restricted loss of mature oligodendrocytes. Stereological quantification of the number of *mbp*:eGFP^{+} somata around the lesion site shows a significant and spatially restricted reduction in the total number of oligodendrocytes at 7 dpl compared to sham controls. Number of experimental animals used were as follows: six for sham control; three for 7 dpl; three for 14 dpl and five for 42 dpl. Data are mean±s.e.m. *P≤0.05 (Kruskal-Wallis followed by Dunn's multiple comparisons post-hoc test). Significance is shown compared to sham control. At 14 and 42 dpl, no significant difference in the number of oligodendrocytes is detected between lesioned and sham control animals. Note that the 7 dpl dataset is the same as presented in Fig. 1C.

Figure S2

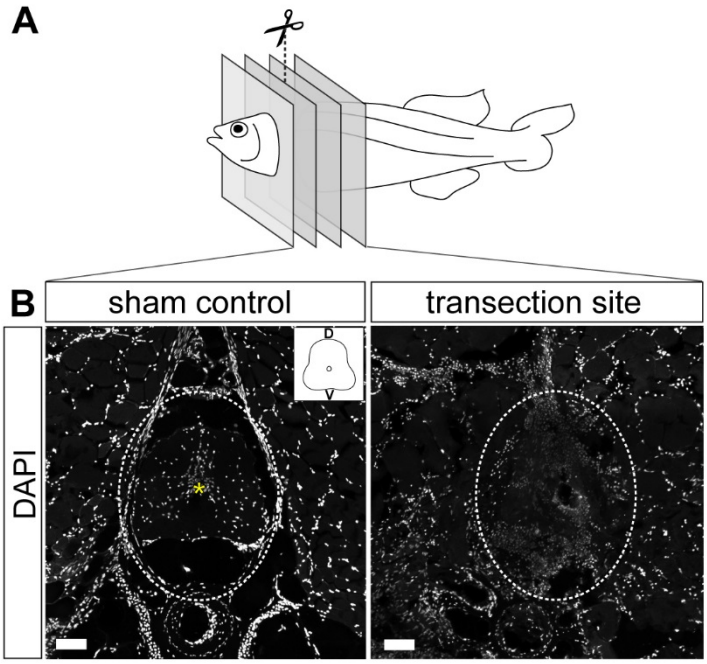

Figure S2. Sample preparation strategy to monitor apoptotic cells in the lesion epicenter. (**A**) After spinal cord lesion, fixed fish are embedded as a whole in cryoblocks and sectioned with a rostral to caudal direction in 12 µm sections. (**B**) Sections are constantly collected until transection site is recognized due to altered tissue morphology. Images shown are maximum intensity projections of transverse sections. D: dorsal; V: ventral. A yellow asterisk indicates the central canal. Scale bars: 100 µm.

Figure S3

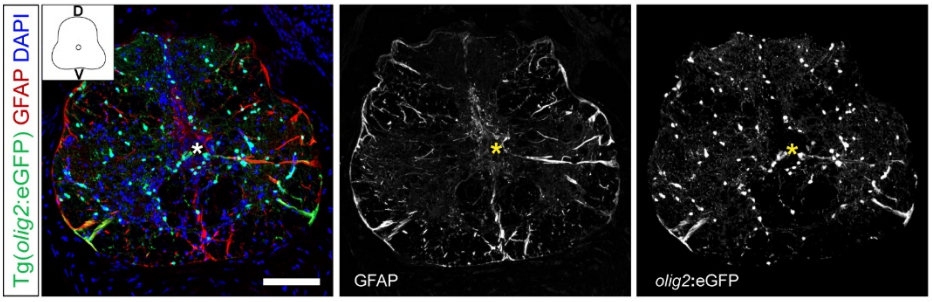

Figure S3. Parenchymal OPCs can be distinguished from *olig2*-expressing ventricular radial glial, based on expression of radial glial markers. In the Tg(o*lig2*:eGFP) line, eGFP is driven by the *olig2* promoter (Shin et al., 2003). In the adult zebrafish spinal cord, *olig2* labels OPCs in the parenchyma and a subset of ventricular radial glia that can be distinguished from parenchymal OPCs based on their size and morphology with long extending processes, markedly lower expression of GFP and expression of radial glia markers ($GFAP^{+}$). Images shown are maximum intensity projections of transverse sections. D: dorsal; V: ventral. In the overview images, a yellow asterisk indicates the central canal. Scale bar: 100 µm.

Figure S4

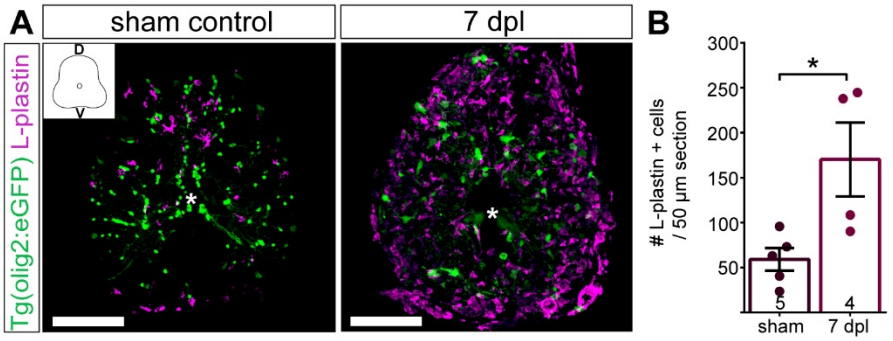

Figure S4. Spinal cord transection results in marked inflammation. (**A**) A marked increase of L-plastin$^+$ cells is detected at 7 dpl. Images shown are maximum intensity projections of transverse sections. D: dorsal; V: ventral. In the overview images, a white asterisk indicates the central canal. Scale bars: 100 µm. (**B**) Stereological quantification of L-plastin$^+$ cells 700 µm around the lesion site shows a significant increase in the number of inflammatory cells at 7 dpl compared to sham controls. Data are mean±s.e.m. Numbers in the plots represent the number of experimental animals. *P≤0.05 (Mann-Whitney test). Significance is shown compared to sham control.

Figure S5

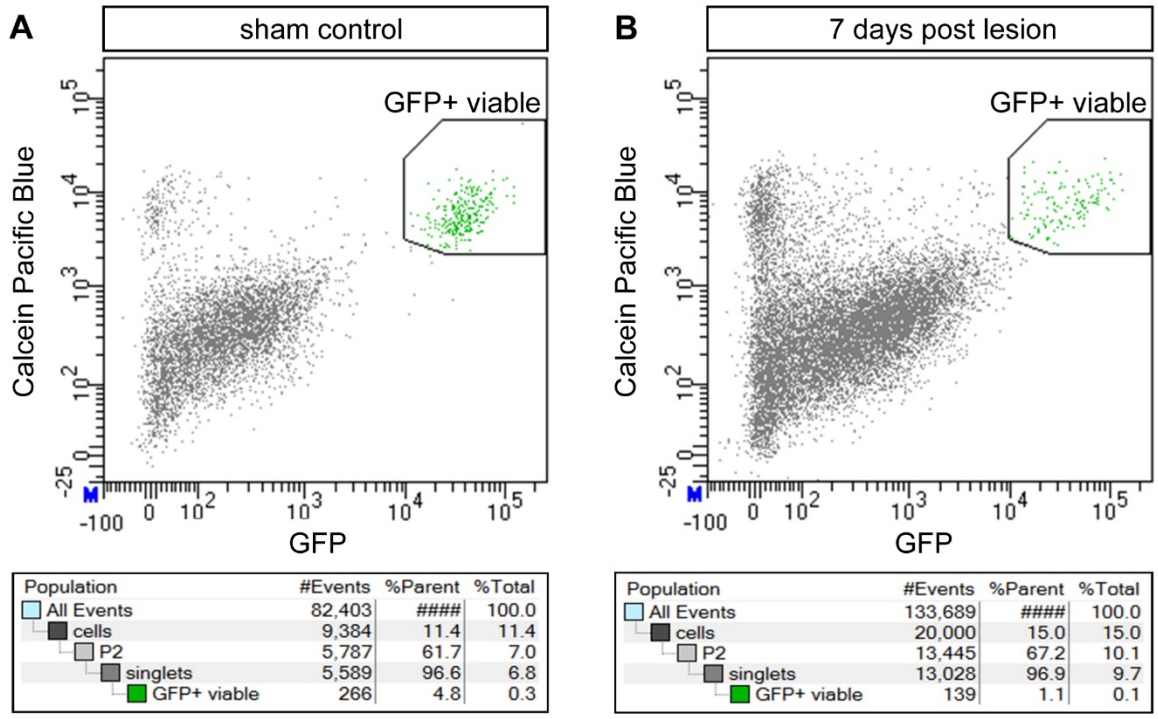

Population	#Events	%Parent	%Total
All Events	82,403	####	100.0
cells	9,384	11.4	11.4
P2	5,787	61.7	7.0
singlets	5,589	96.6	6.8
GFP+ viable	266	4.8	0.3

Population	#Events	%Parent	%Total
All Events	133,689	####	100.0
cells	20,000	15.0	15.0
P2	13,445	67.2	10.1
singlets	13,028	96.9	9.7
GFP+ viable	139	1.1	0.1

Figure S5. Fluorescence activated cell sorting (FACS) of OPCs from ~ 0.5 mm of spinal cord tissue in sham control (**A**) **and 7 dpl** (**B**) **fish.** Gating of OPCs was based on endogenous expression of eGFP and counter stain signal of Calcein Blue AM Dye to sort for viable cells in sham control and 7 dpl groups, respectively**.**

Figure S6

A

Sample	Intragenic		Intergenic	Expression Efficiency	Transcripts	Genes
	Extronic	Intronic				
sham	0,787±0,005	0,114±0,002	0,098±0,003	0,774±0,005	21.223±513,6	10.055±252,3
7 dpl	0,805±0,002	0,104±0,001	0,091±0,001	0,791±0,002	26.904±457,9	12.862±244,1

B

Sample	Total Fragments	Assigned	%
sham	$10.61x10^7$±415.514	$8.226x10^6$±294.066	77,64±0,501
7 dpl	$10.55x10^7$±239.918	$8.404x10^6$±199.449	79,62±0,245

C

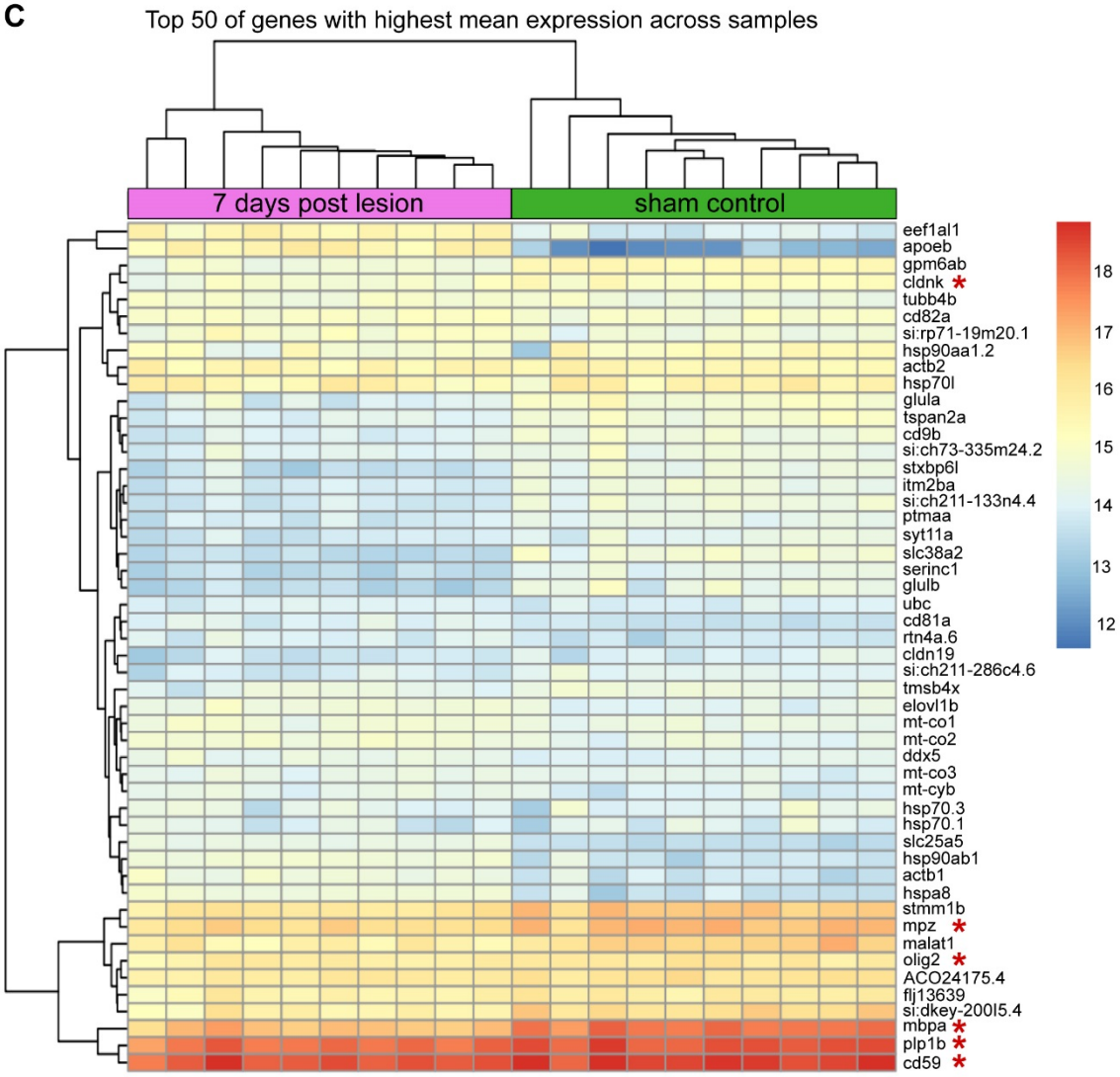

D

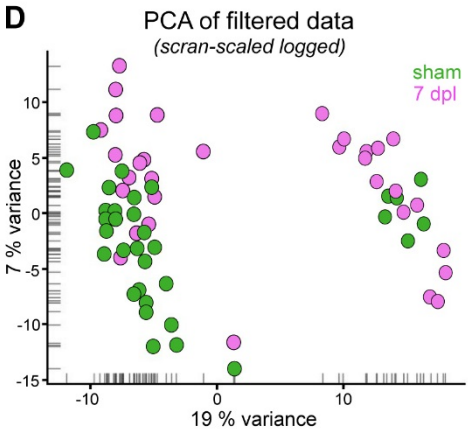

E

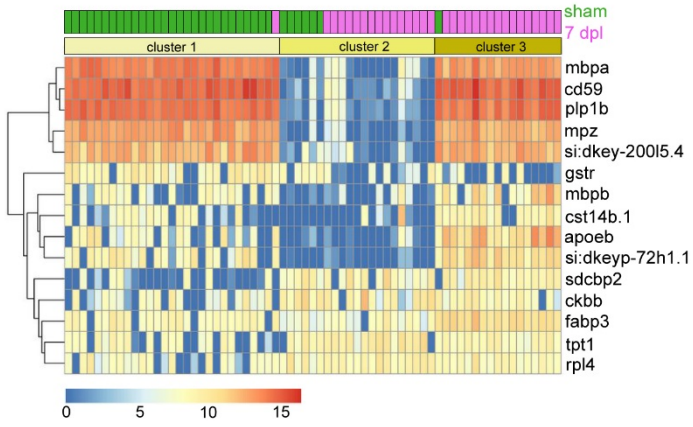

Figure S6. Sample profile, fragment counts and heatmap of genes with highest mean expression across samples (50 genes). (**A**) Sample Profile. The table shows the proportion of reads in exonic, intronic and intergenic regions and the expression efficiency based on the reads in exonic regions. Furthermore, an approximation of the total number of genes and transcripts is provided. (**B**) Fragment Counts. The amount of fragments which are uniquely aligned and within an exonic region is shown (in total number and percentage). (**C**) The normalized fragment counts of the genes are transformed and the mean value across all samples is calculated. This is done for all genes and then the genes with the highest mean are selected. The scale goes from blue to red, with red meaning the highest expression. Typical expected genes for OPCs are indicated with red asterisks. (**D**) Principal component analysis (PCA) of filtered data after single-cell RNAseq of reactive (7 dpl) vs sham control OPCs. Basic gene filtering occurred after filtering mitochondrial genes, rRNA genes and genes with counts in less than 10 cells. Upon filtering, 5,033 genes remained. (**E**) Metacell clustering of differentially expressed genes (DEGs) between reactive and sham OPCs.

Figure S7

Ensemble ID	Gene Symbol	Gene name	log2 Fold Change	*p* value
ENSDARG00000087804	*tnfrsf11a*	tumor necrosis factor receptor superfamily, member 11a, NFKB activator	2.68	0.0007363939
ENSDARG00000056627	*cxcl14*	chemokine (C-X-C motif) ligand 14	8.14	2.483392E-38
ENSDARG00000102583	*il4r.1*	interleukin 4 receptor, tandem duplicate 1	2.21	0.003458611
ENSDARG00000015902	*stat6*	signal transducer and activator of transcription 6, interleukin-4 induced	2.59	0.001042094

Figure S7. Reactive OPCs upregulate genes involved in immune system function. Selection of DEGs involved in immune system function, shown to be upregulated in reactive vs. non-reactive OPCs at 7 dpl.

REFERENCES

Handschuh S (2013) A correlative approach for combining microCT, light and transmission electron microscopy in a single 3D scenario. . Front Zoology.

Metscher DB (2009) MicroCT for developmental biology: a versatile tool for high-contrast 3D imaging at histological resolutions. Developmental dynamics : an official publication of the American Association of Anatomists.

Minarik M (2017) Pre-oral gut contributes to facial structures in non-teleost fishes. Nature.

Munzel EJ, Schaefer K, Obirei B, Kremmer E, Burton EA, Kuscha V, Becker CG, Brosamle C, Williams A, Becker T (2012) Claudin k is specifically expressed in cells that form myelin during development of the nervous system and regeneration of the optic nerve in adult zebrafish. Glia 60:253-270.

Shin J, Park HC, Topczewska JM, Mawdsley DJ, Appel B (2003) Neural cell fate analysis in zebrafish using olig2 BAC transgenics. Methods Cell Sci 25:7-14.

Venable JH, Coggeshall R (1965) A SIMPLIFIED LEAD CITRATE STAIN FOR USE IN ELECTRON MICROSCOPY. The Journal of cell biology 25:407-408.